TECHNISCHE
UNIVERSITÄT
MÜNCHEN

WALTHER-MEISSNER-
INSTITUT FÜR TIEF-
TEMPERATURFORSCHUNG

BAYERISCHE
AKADEMIE DER
WISSENSCHAFTEN

On-chip Superconducting Microwave Interferometer

Master's Thesis

Michael Fischer

Supervisor: Prof. Dr. Rudolf Gross

München, December 2014

Fakultät für Physik
Technische Universität München

Contents

1. Introduction

In the last few years, scientists have made great progress towards using circuit quantum electrodynamics (QED) [1] for quantum information processing (QIP)[2]. Proof-of-concept experiments have already been performed for both quantum computation [3] and quantum simulation [4]. In circuit QED, photons inside of superconducting transmission lines and resonators interact with artificial atoms, called qubits [5, 6]. The different parts are implemented in a solid-state architecture. In contrast to its optical counterpart, cavity QED [7, 8], circuit QED allows on the one hand for easy access to large coupling strengths between photons and qubits [9, 10], in addition to good scalability. On the other hand, the coherence time of superconducting qubits is much smaller than that of isolated atoms in cavities, due to two level systems in the solid state environment. Nonetheless, recent research has lead to higher and higher qubit coherence times, thus enabling a large amount of coherent operations on multiple qubits [11, 12]. In solid-state architectures, qubits are built using Josephson junctions [13], which add a nonlinearity to the system. The latter is used to create quasi two level systems, acting as artificial atoms. Josephson circuits offer an *in-situ* tunability [14]. As a new approach to QIP, the qubit information can be encoded in a dual-rail setup, consisting of two transmission lines. Similarly to all-optical quantum computing [15], the qubit states are superpositions of a microwave photon travelling in either one of the transmission lines. In QIP, operations between multiple qubits are needed to perform algorithms used in quantum computation. In order to use the dual-rail setup, these so called gates need to be implemented for two dual-rail encoded qubits. One important two qubit gate, a controlled phase gate, can be built with an interferometer equipped with a photon number dependent phase shifter. In this situation, the two transmission lines must be part of two different dual-rail encoded qubits. [15]. The goal of this thesis is to build on-chip interferometers for the application in a controlled phase gate. To achieve this, we perform theoretical calculations and simulations and finally measure the devices. In chapter 2, we explain the theoretical background, that is needed to understand the fundamental component of a controlled phase gate, i.e., an interferometer, which consists of two beam

splitters linked by transmission lines. In chapter 3, we present the measurement setup and the fabrication of an interferometer. Chapter 4 shows simulations of different beam splitters and interferometers used to explain our measurement results. In this chapter, we also discuss different ideas and variations of our designs, which are expected to improve future measurements. Measurements of three interferometer chips are analyzed in chapter 5. The results of the thesis are summarized in chapter 6, where we also give an outlook on future measurements towards a controlled phase gate.

2. Theory

In this chapter, the theoretical background of this work is shown. We begin with a introduction to microwave technology, including coplanar waveguides and scattering parameters. Next, the theory of a beam splitter is presented and finally the theory of an interferometer is discussed.

2.1. Microwave Technology

In general, broadband microwave devices are built using transmission lines. The latter consist of at least two conductors, which are separated by a gap. Along these transmission lines, electromagnetic waves can propagate. There exist various transmission line types, for example, slotlines, microstrips and coplanar waveguides. The devices investigated in this thesis are all of the coplanar waveguide (CPW) design, which is shown in Fig. 2.1. The CPW structure consists of an inner conductor of width W and two outer conductor ground planes which are separated from the inner conductor by two gaps of width G. The conductors are thin metallic layers with a thickness d on a substrate material of height H and a relative dielectric constant ϵ_r. The materials used in this thesis are niobium and silicon. Important to note is, that the spatial distribution of the electromagnetic field strongly depends on the transmission line type. This is relevant when coupling artificial atoms to the transmission line. In this respect, CPWs are advantageous compared to other geometries since the electric field is concentrated in the gap where an artificial atom coupling to electric fields can be placed. The main mode of the electric field in a CPW is shown in Fig. 2.2. The mode is a quasi transverse electromagnetic (TEM) mode. In a TEM mode, the electric and magnetic field are perpendicular to the direction of propagation of the field. Quasi TEM means, that the wave travels through two media with different relative dielectric constants. In a transmission line other modes can exist as well. These additional modes can couple to the main mode

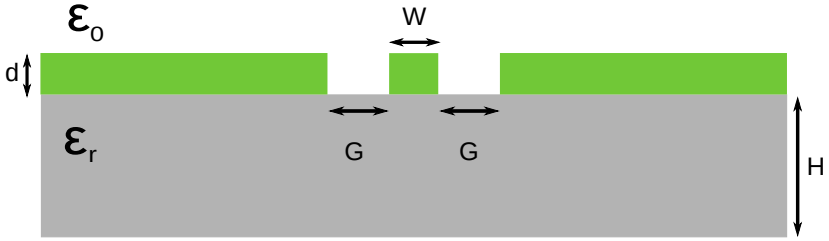

Figure 2.1: Cross section of a CPW, with the metal layer and substrate coloured in green and gray, respectively.

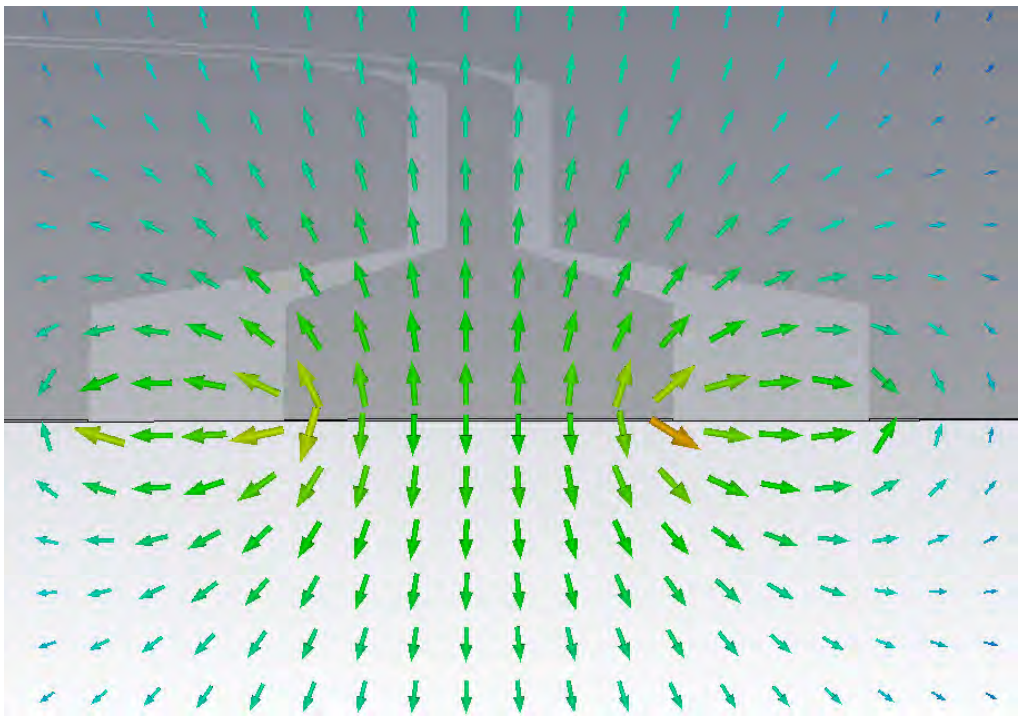

Figure 2.2: Simulation of the electric field (arrows) of the fundamental mode in a coplanar waveguide depicted in the plane perpendicular to the propagation direction, performed with CST microwave studio.

and impair its transmission properties. An example for this is, that different potentials at the ground planes can lead to slotline modes (see Sec. 4.1).

2.1.1. Impedance of a CPW

The impedance of a transmission line is defined as

$$Z_0 \equiv \frac{V_0^+}{I_0^+} = \sqrt{\frac{L_l}{C_l}}, \tag{2.1}$$

where V_0^+ and I_0^+ are the phasors of voltage and current of an incident wave and L_l and C_l are the inductance and capacitance per unit length. The second part of the equation is only true for a lossless line and approximately valid for low loss lines. For the equations describing the dependence of the impedance Z_0 on the geometric parameters, we point the reader to Ref. [16]. For simple cases, we make use of the software TX-LINE to estimate the impedance [17]. For more complex geometries, such as conductor backed CPWs with vias, software applying the finite element method [see Sec. 2.5] is required. In an ideal measurement setup, the impedance of all components is equal to the same value, typically $50\,\Omega$, unless it is especially desired to have a varying impedance [see Sec. 2.3]. Discontinuities of the impedance, i.e., impedance mismatches, lead to reflections described by the reflection coefficient Γ (see Ref. [16]):

$$\Gamma = \frac{Z_1 - Z_0}{Z_1 + Z_0}. \tag{2.2}$$

Two sites with impedance mismatches can behave as an harmonic oscillator. The resonant frequency of this harmonic oscillator, or resonator, can be written as

$$\omega_{\text{resonator},1} = \frac{2\pi \cdot c}{\sqrt{\epsilon_{\text{eff}}} \cdot 2 \cdot l_{\text{resonator}}}. \tag{2.3}$$

Here, ϵ_{eff} is the effective dielectric constant of the transmission line, $l_{\text{resonator}}$ is the length of the transmission line between the two sites and c is the speed of light in vacuum. ϵ_{eff} is a combination of the two dielectric constants of the two materials below and above the metal layer.

A similar phenomenon can appear at distinct frequencies given by the geometry of the chip, where standing waves can build between the edges. For further informations and simulations of those waves see among others Sec. 4.2.

2.2. Scattering parameter

A convenient way to describe a microwave device under test is its scattering matrix. The matrix contains all scattering parameters (S-parameters), which each describe the behaviour of the device if it is only excited at one port. For example, S-parameter S_{21} is the part of the wave that is measured at port 2 if a wave is excited at port 1. If V_i^+ is the voltage phasor of the incident wave at port i and V_i^- the one of the reflected wave at port i, the S-parameter matrix S of a device with four ports [as seen in Fig. 2.3] is defined as

$$\begin{pmatrix} V_1^- \\ V_2^- \\ V_3^- \\ V_4^- \end{pmatrix} = S \cdot \begin{pmatrix} V_1^+ \\ V_2^+ \\ V_3^+ \\ V_4^+ \end{pmatrix} = \begin{pmatrix} S_{11} & S_{12} & S_{13} & S_{14} \\ S_{21} & S_{22} & S_{23} & S_{24} \\ S_{31} & S_{32} & S_{33} & S_{34} \\ S_{41} & S_{42} & S_{43} & S_{44} \end{pmatrix} \cdot \begin{pmatrix} V_1^+ \\ V_2^+ \\ V_3^+ \\ V_4^+ \end{pmatrix}. \tag{2.4}$$

The scattering parameter is defined as

$$S_{ij} = \frac{V_i^-}{V_j^+} \quad \text{while} \quad V_k^+ = 0 \quad \text{for} \quad k \neq j. \tag{2.5}$$

In most cases S-parameters are dependent on the frequency of the incoming wave. Therefore, it is often important to measure the frequency dependence of S-parameters. For example, the resonant structures described in Sec. 2.1.1 can be seen in a transmission measurement of a system that couples to the resonant structure (e.g., the measurement of S_{21}) as dips at their resonant frequencies. As one aims for a smooth transmission without features that do not originate from the actual device, it is very important to avoid possible impedance mismatches. To better handle the common exponential dependence of S-parameters on, e.g., length, they are often given in units of decibels.

$$S_{ij}[\text{dB}] = 10 \cdot \log\left(|S_{ij}|^2\right). \tag{2.6}$$

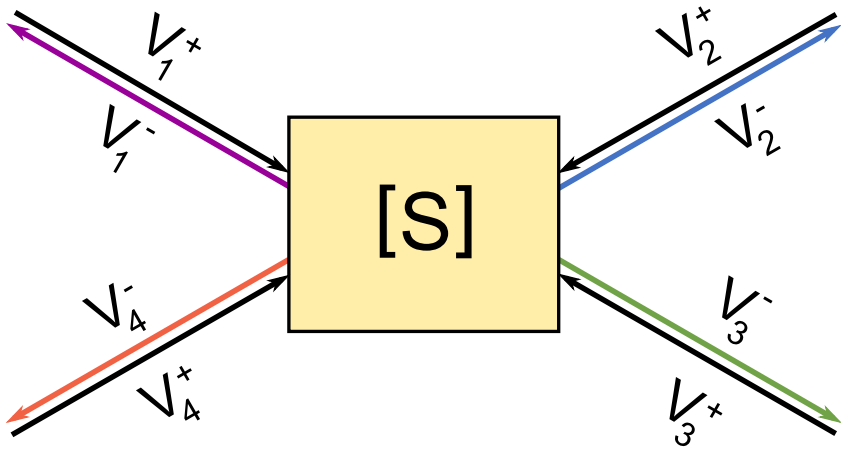

Figure 2.3: Schematic of a four port device with the voltage phasors for each port.

2.3. Beam splitter

A beam splitter is a device that splits an incoming wave into two parts propagating along separate paths. In this thesis, we focus on beam splitters, where both outgoing waves contain half the power of the incoming wave. In case of a 90° hybrid coupler, there is a 90° phase shift between the two outgoing waves. The beam splitter used in this thesis is a 4-port device with one input port, two output ports and an isolation port [see Fig 2.4]. We will refer to the transmission to these ports as reflection (port 1), straight transmission (port 2), cross transmission (port 3) and isolation (port 4). The S-parameter matrix for a 90° hybrid is given by

$$S = \frac{-1}{\sqrt{2}} \begin{bmatrix} 0 & i & 1 & 0 \\ i & 0 & 0 & 1 \\ 1 & 0 & 0 & i \\ 0 & 1 & i & 0 \end{bmatrix}. \tag{2.7}$$

The beam splitters, that are used in this thesis, are interference devices, which indicates, that they have an optimal working frequency. Therefore, the intended behaviour only occurs in an interval around this frequency. The S-parameter matrix shown above is only exactly valid at the working frequency. In a measurement of the transmission through a beam splitter we anticipate a transmission of $-3\,\mathrm{dB}$ at the working frequency for ports 2 and 3 and perfect isolation for ports 1 and 4. A sketch of a beam splitter that can theoretically achieve this, is shown in Fig. 2.4 [18]. The behaviour is achieved through the geometry of the square formed by transmission lines. Two of the sides of

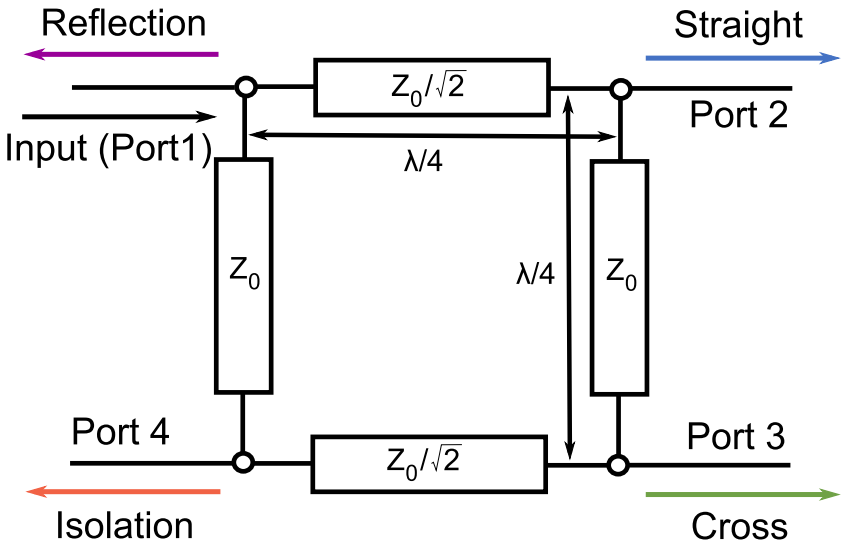

Figure 2.4: Schematic of a beam splitter.

the square are at an impedance of $Z_0 = 50\,\Omega$, which is also the impedance of the feed lines. The other two are at $Z_0/\sqrt{2} \approx 35.4\,\Omega$. All four are of the length $\lambda/4$, where λ is the wavelength of the desired working frequency. Since λ changes with the geometry and impedance of the transmission line, the length for the $50\,\Omega$ arms differs slightly from the ones with $35.4\,\Omega$. The 90° hybrid provides an advantageous port configuration since both output ports can be easily placed on the same side next to each other, which is of good use for cascading multiple devices in a planar geometry without crossing transmission lines.

With the help of even-odd-mode analysis one can analyze the frequency dependence of the beam splitter. For this analysis, the system is excited by an even and an odd mode. The voltage phasors of these two modes are

$$V^+_{1,\text{even}} = \frac{1}{2} \quad \text{and} \quad V^+_{4,\text{even}} = \frac{1}{2}, \tag{2.8}$$

$$V^+_{1,\text{odd}} = \frac{1}{2} \quad \text{and} \quad V^+_{4,\text{odd}} = -\frac{1}{2}. \tag{2.9}$$

Thanks to the symmetric structure of the beam splitter, we can convert the four port device into a two port device by replacing the transmission lines between port 1 and 4 and port 2 and 3 with two open or short lines of half length for the even and odd mode, respectively. In addition to scattering matrices, two port devices can be described by

transmission matrices, defined as

$$\begin{pmatrix} V_1^+ \\ I_1^+ \end{pmatrix} = \begin{pmatrix} A & B \\ C & D \end{pmatrix} \cdot \begin{pmatrix} V_2^- \\ I_2^- \end{pmatrix}. \tag{2.10}$$

They are especially useful for the description and calculation of systems, that consist of multiple cascaded subsystems. If we know the transmission matrices for each subsystem, a transmission matrix for the whole system can be calculated by using matrix multiplication. For the treated beam splitter, these subsystems are empty transmission lines and lines with open or shorted arms. The transmission matrices T for these systems are [16]:

$$\mathrm{T}_{\mathrm{open}} = \begin{pmatrix} 1 & 0 \\ \frac{-i}{\mathrm{Z}} \cot(\frac{2\pi}{\lambda} l) & 1 \end{pmatrix} \tag{2.11}$$

$$\mathrm{T}_{\mathrm{short}} = \begin{pmatrix} 1 & 0 \\ \frac{i}{\mathrm{Z}} \tan(\frac{2\pi}{\lambda} l) & 1 \end{pmatrix} \tag{2.12}$$

$$\mathrm{T}_{\mathrm{transmission}} = \begin{pmatrix} \cos(\frac{2\pi}{\lambda} l) & i\mathrm{Z} \sin(\frac{2\pi}{\lambda} l) \\ \frac{i}{\mathrm{Z}} \sin(\frac{2\pi}{\lambda} l) & \cos(\frac{2\pi}{\lambda} l) \end{pmatrix}. \tag{2.13}$$

Z is here the respective impedance of the lines, λ is the wavelength of the wave in the system and l is the length of the considered part. We can combine these matrices to receive the description for the two excitations of the beam splitter.

$$\mathrm{T}_{\mathrm{bs,even}} = \mathrm{T}_{\mathrm{open}} \cdot \mathrm{T}_{\mathrm{transmission}} \cdot \mathrm{T}_{\mathrm{open}} \tag{2.14}$$

$$\mathrm{T}_{\mathrm{bs,odd}} = \mathrm{T}_{\mathrm{short}} \cdot \mathrm{T}_{\mathrm{transmission}} \cdot \mathrm{T}_{\mathrm{short}} \tag{2.15}$$

The even and odd excitations are calculated individually and are converted into S-parameters. The formula for the calculation of S_{21} is

$$\mathrm{S}_{21} = \frac{2(\mathrm{AD} - \mathrm{BC})}{\mathrm{A} + \frac{\mathrm{B}}{\mathrm{Z}} + \mathrm{CZ} + \mathrm{D}}. \tag{2.16}$$

The other scattering parameters can be calculated similarly ([16] table 4.2), leaving us with four S-parameters for the even and four S-parameters for the odd mode. Using these S-parameter extracted from the even-odd mode analysis of the two port systems, we can calculate the voltage phasors V_i^- for all four initial ports, thus leading to a frequency dependent description of the four port system. For further information, we

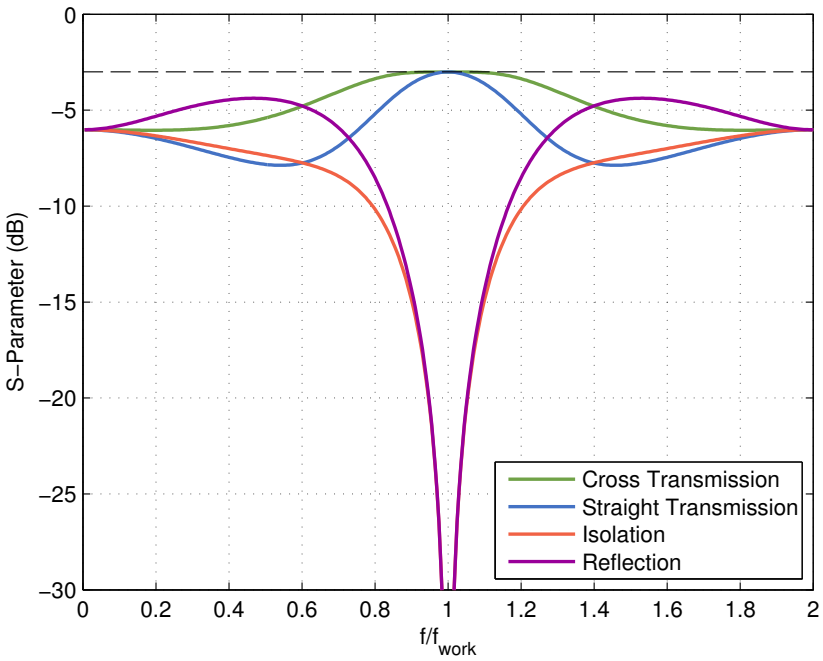

Figure 2.5: Theoretical behaviour of a beam splitter. Calculated using even-odd-mode analysis.

refer the interested reader to Ref. [16].

The results of the even-odd mode analysis for the beam splitter are displayed in Fig. 2.5. In the vicinity of the working frequency (f_{work}) we obtain the desired behaviour. For higher and lower frequencies the isolation of the input and isolation port is lost and the device can not be used as a beam splitter any longer. Nevertheless, the usable bandwidth of the device for an isolation level of 20 dB is $0.1 \cdot f_{work}$ which, for a working frequency of 5.75 GHz, is much larger than the one of superconducting resonators (several MHz to tens of MHz) used to generate single microwave photons.

Using even-odd mode analysis, we can now also take a look at the dependence of the behaviour of the beam splitter when introducing a small deviation of impedance in the arms of the beam splitter. Exemplary, we will consider a slightly smaller and a slightly larger impedance in the beam splitter arms with the original impedance of $Z_0/\sqrt{2} \approx 35.4\,\Omega$. Changing the impedance by $2\,\Omega$ already shows significantly altered behaviour [see Fig. 2.6]. Independent of the sign of the impedance shift, we no longer observe perfect behaviour for the isolation and reflection around the working frequency, but a transmission of approximately -25 dB at both ports. For an impedance of $33.4\,\Omega$, we find an increased transmission of -2.6 dB at the straight port and a decreased transmission

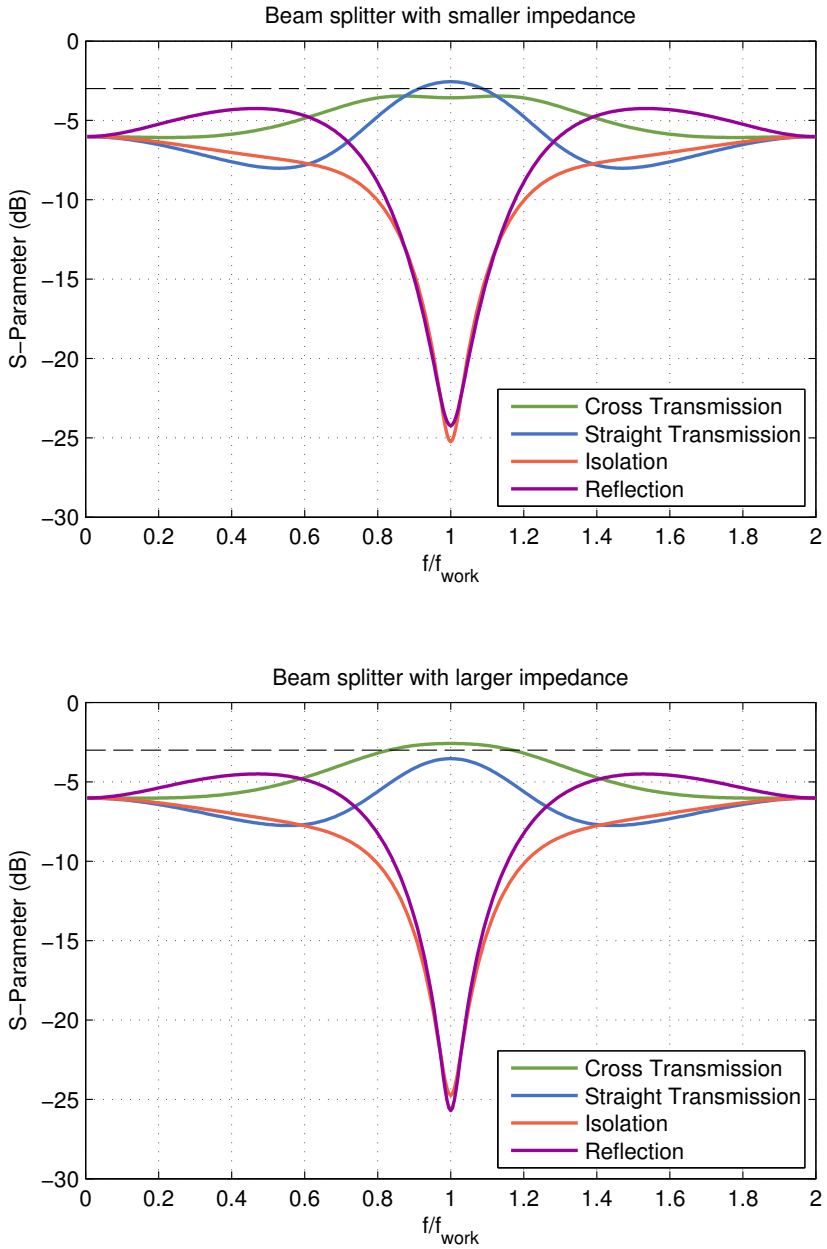

Figure 2.6: Theoretical behaviour of a beam splitter with altered impedance in two arms. Top panel: impedance reduced by 2 Ω. Bottom panel: impedance increased by 2 Ω.

of −3.6 dB at the cross port [Fig. 2.6, top panel]. For an impedance of 37.4 Ω, we observe an opposite trend [see Fig. 2.6, bottom panel]. This leads to the conclusion, that even small impedance mismatches inside the beam splitter have a large impact on the behaviour around the working frequency of the system.

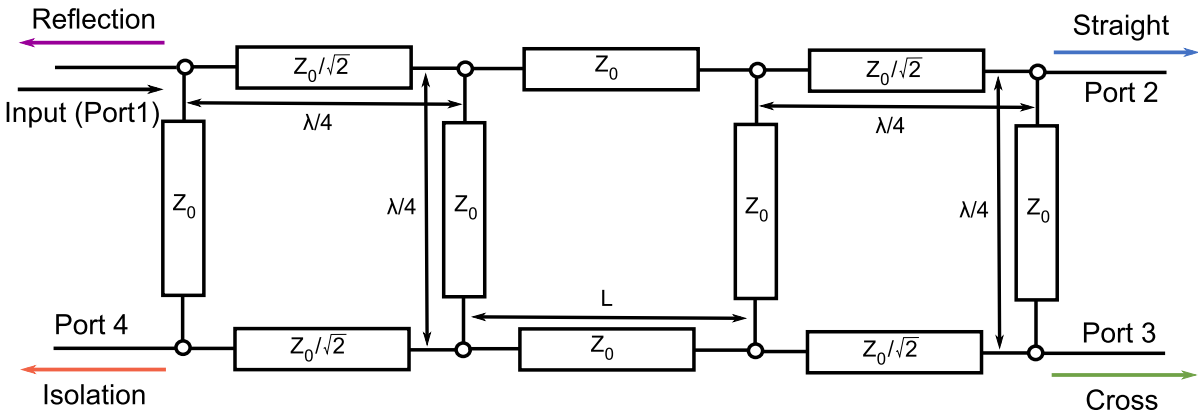

Figure 2.7: Sketch of an interferometer built with two beam splitters.

2.4. Interferometer

The interferometer is one of the basic components of a controlled phase gate. At the working frequency of an interferometer an incoming wave at port 1 is transmitted without loss to port 3. The phase shift between the incoming and outgoing wave is 180°. The S-parameter matrix for such a device is

$$S = \begin{bmatrix} 0 & 0 & -1 & 0 \\ 0 & 0 & 0 & -1 \\ -1 & 0 & 0 & 0 \\ 0 & -1 & 0 & 0 \end{bmatrix}. \tag{2.17}$$

Interferometers can be build by cascading two beam splitters [see Fig. 2.7]. Similar to the treatment of the beam splitter one can use even-odd-mode analysis to determine the frequency dependence. The transmission matrices for the even and odd excitation of the interferometer can be calculated using formula 2.14 and 2.15:

$$\mathrm{T}_{\mathrm{if,even}} = \mathrm{T}_{\mathrm{bs,even}} \cdot \mathrm{T}_{\mathrm{transmission}} \cdot \mathrm{T}_{\mathrm{bs,even}} \tag{2.18}$$

$$\mathrm{T}_{\mathrm{if,odd}} = \mathrm{T}_{\mathrm{bs,odd}} \cdot \mathrm{T}_{\mathrm{transmission}} \cdot \mathrm{T}_{\mathrm{bs,odd}}. \tag{2.19}$$

$\mathrm{T}_{\mathrm{transmission}}$ is the transmission matrix for the transmission line connecting the two beam splitters. $\mathrm{T}_{\mathrm{transmission}}$ depends on the impedance Z and length L of this joint. With this it is possible to calculate the S-parameters of the interferometer. A plot of all S-parameters for a working frequency of 5.75 GHZ and a joint length of L = 0 is shown in Fig. 2.8. The calculations show a perfect behaviour at the working frequency, but the desired

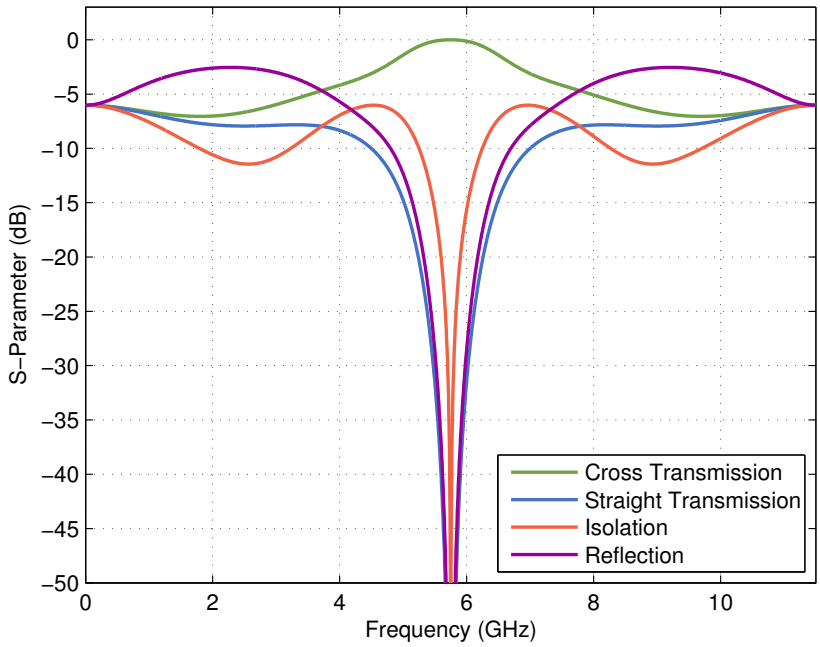

Figure 2.8: Theoretical behaviour of an interferometer. Calculated by using even-odd-mode analysis for a working frequency of 5.75 GHz and L = 0.

behaviour is quickly lost for lower and higher frequencies.

The impedance in the arms with a nominal impedance of $Z_0/\sqrt{2}$ of the beam splitter has a big effect on the outcome of the theoretical calculation of the beam splitter [see Sec. 2.3]. Therefore, it is important to see whether this impedance mismatch impacts the interferometer similarly. The calculations show, that the reflection and the straight transmission increase to approximately $-19\,\mathrm{dB}$ for an impedance mismatch of $2\,\Omega$ [Fig. 2.9]. The isolation increases to $-38\,\mathrm{dB}$ and the cross transmission is decreased by approximately $0.1\,\mathrm{dB}$. A decrease in impedance in the $Z_0/\sqrt{2}$-arms, also leads to additional dips in reflection and straight transmission [see Fig. 2.9, top panel].

Another crucial factor for the behaviour of the interferometer is the transmission line length between the two beam splitters. The calculations show, that the scattering parameters strongly depend on the latter [see Fig. 2.10]. For a length $L = \lambda_{\mathrm{work}}/4$, the shape is symmetric. The dip in isolation and straight transmission at the working frequency is broadened in comparison to the case of L = 0, leading to a larger interval where the signal is almost exclusively transmitted to the cross port. A length greater than zero, but different from multiples of $\lambda_{\mathrm{work}}/4$, leads to an asymmetrical behaviour

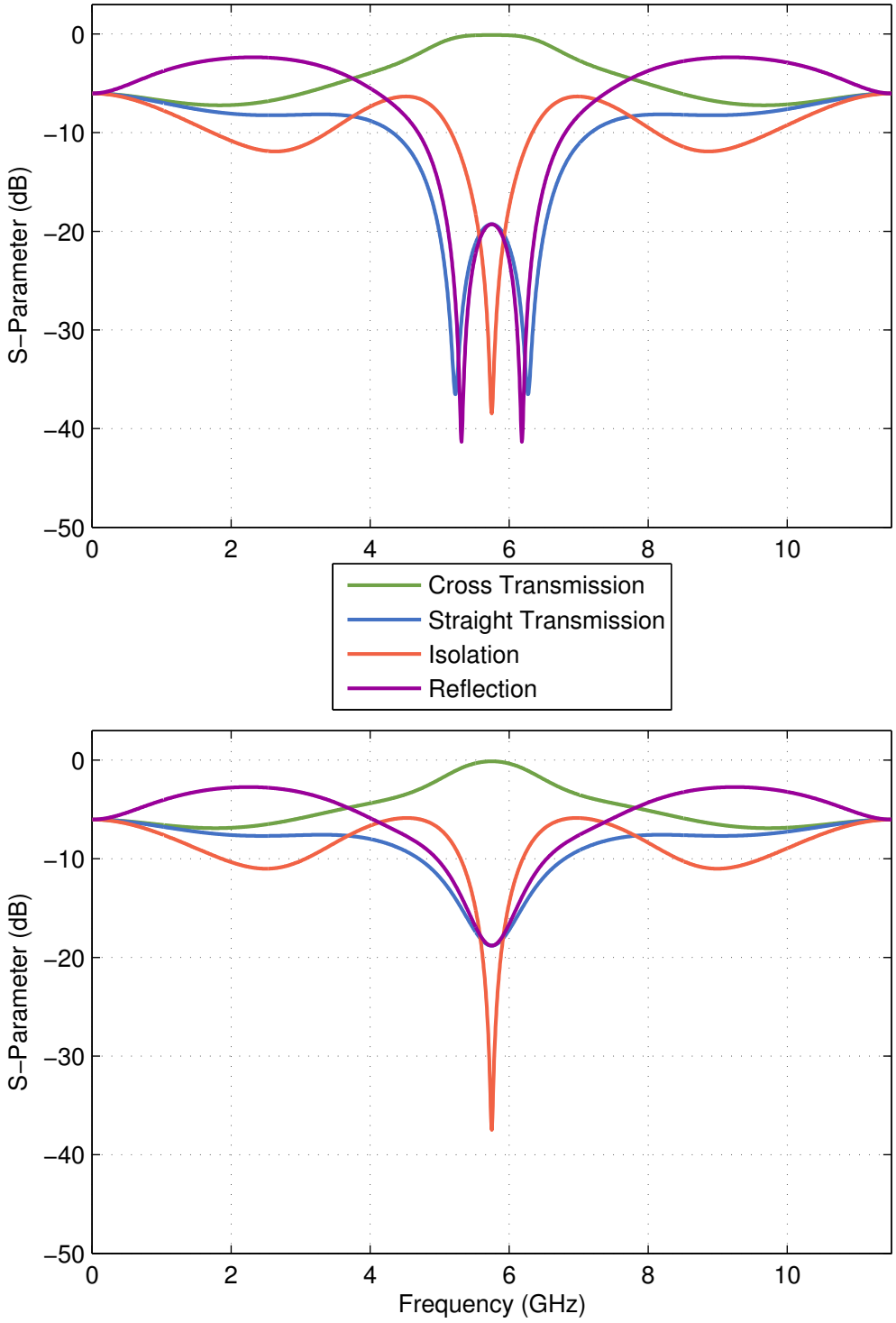

Figure 2.9: Theoretical behaviour of an interferometer with altered impedance in the beam splitter arms of nominal length $Z_0/\sqrt{2}$. Top panel: impedance reduced by $2\,\Omega$. Bottom panel: impedance increased by $2\,\Omega$. Calculated by using even-odd-mode analysis for a working frequency of $5.75\,\mathrm{GHz}$ and $L = 0$.

of the S-parameters. For example, a length L = $0.8\lambda_{\text{work}}/4$ generates an additional dip in the straight transmission and in the isolation at 6.3 GHz [Fig. 2.10, bottom panel]. The location of this dip depends on L. For L > $\lambda_{\text{work}}/4$, the dip is observed at lower frequencies than the working frequency.

2.5. Finite element method

Simulations are helpful to gain more information about complex systems with complicated geometry. In this thesis, simulations have been performed with CST microwave studio [19], a simulation program, that uses finite element method. With this numerical method, complex problem types, such as systems that are described by partial differential equations (PDE), can be simplified to allow faster simulation of the system. The finite element method discretizes the spatial components of the system by splitting the simulated area into a finite number of mesh cells. The simulations in this thesis use a hexahedral mesh, which divides the model into cuboids (see Fig. 2.11). The first step to reduce the problem from a partial differential equation to a set of ordinary differential equations (ODE), is to approximate the solution of the PDE by a linear combination of basis functions [20]

$$u_{\text{approx}}(t,x) = \sum_{j=1}^{n} \alpha_j(t)\phi_j(x). \tag{2.20}$$

Here, $\alpha_j(t)$ denote time dependent coefficients and $\phi_j(x)$ the spatial dependent basis functions. In this way, the space and time variables are separated. Using the discretization of the spatial dependence we demand, that the approximated function is a solution for the equation in question for discrete points x_i, with $i = 1, ..., n$. This leads us to n ODEs for the coefficients a_j. These ODEs can then be converted into a matrix description, that can be calculated more easily by a computer. The accuracy of the simulation can be increased with a higher number of mesh cells which leads to a better spatial resolution. Especially at curves in transmission lines or at transitions between different materials, a high number of mesh cells is crucial for a good result of the simulation. Therefore, the simulations use an iterative process to improve the mesh cell number and placement. An important criterion to judge the accuracy of this method is the convergence of the simulated parameters.

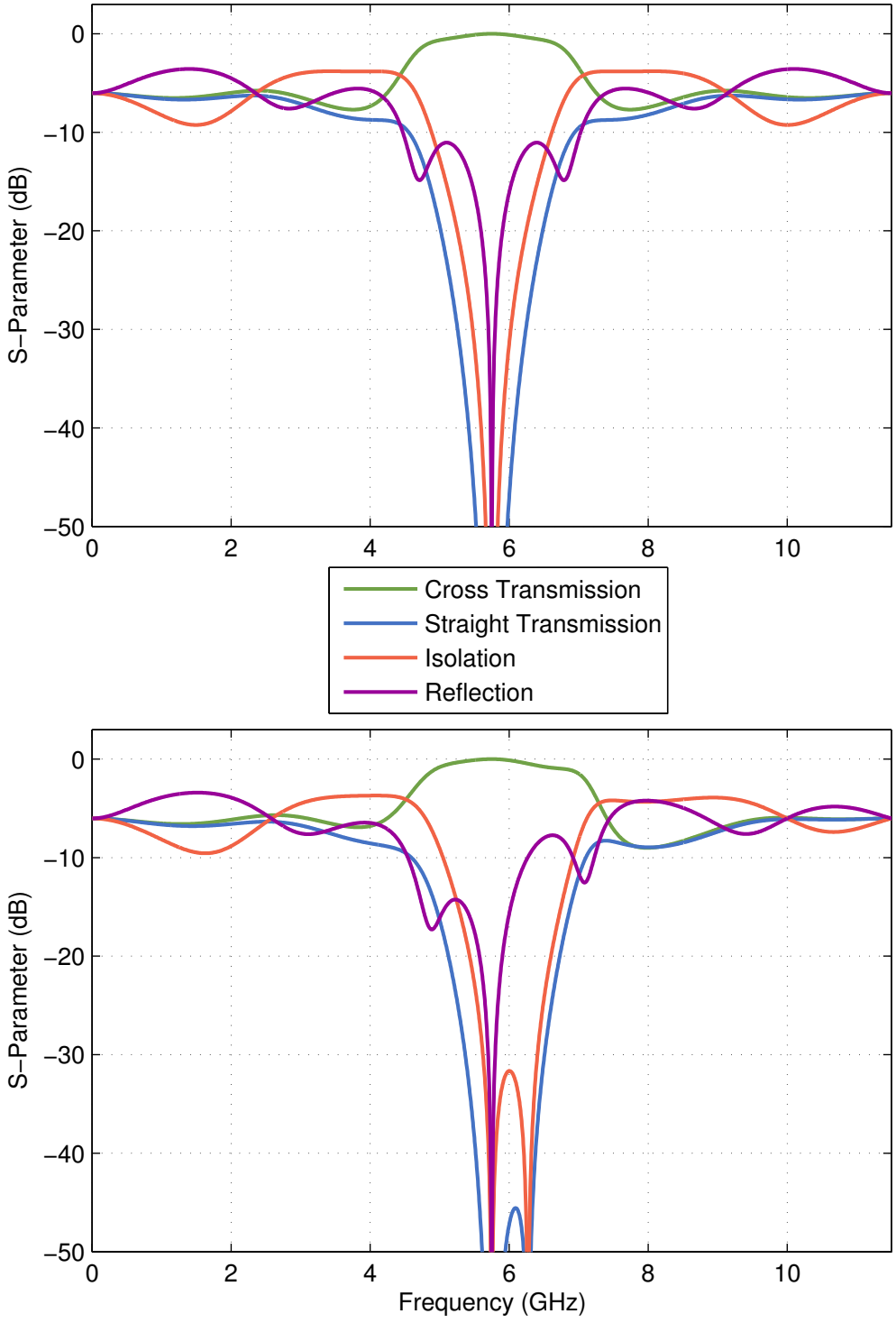

Figure 2.10: Theoretical behaviour of an interferometer with altered length between the beam splitters. Top panel: $L = \lambda_{work}/4$. Bottom panel: $L = 0.8 \cdot \lambda_{work}/4$. Calculated by using even-odd-mode analysis for a working frequency of 5.75 GHz.

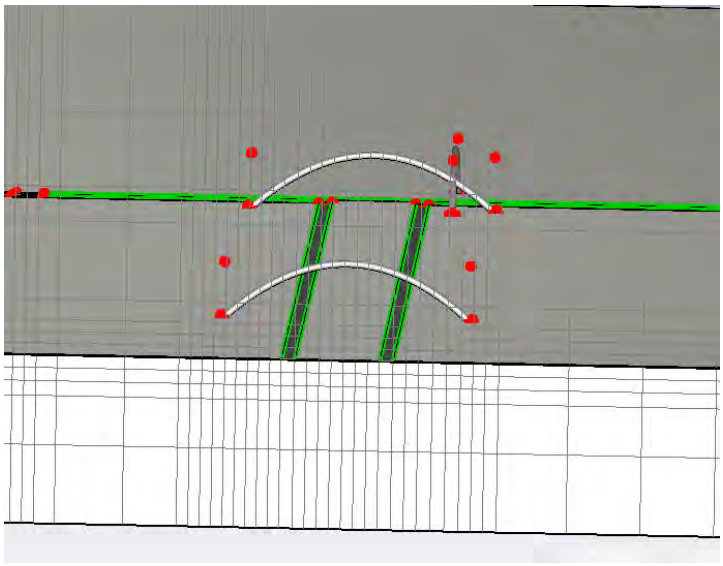

Figure 2.11: Cut through a model of a beam splitter with displayed mesh cells. The silicon waver is shown in white, the niobium layer in gray and the aluminium bonds are silver. The red and green marked lines and points are used by the simulation software for the mesh calculation.

3. Experimental techniques

In this chapter, we take a closer look at the experimental techniques necessary to perform the measurements in this thesis. First the sample fabrication is described, followed by an overview of the setup for cryogenic transmission measurements among others consisting of the cryostat itself, a measurement box and printed circuit boards. At the end of the chapter, calibration measurements are shown.

3.1. Sample fabrication

The measured devices are structured from niobium coated silicon chips. The silicon chips are 250 µm thick and the niobium layer thickness is 100 nm. The niobium layer is put on the silicon layer in a niobium sputtering chamber [Fig. 3.1(a)], which deposits the wanted thickness in four minutes. After a standard cleaning process including acetone and isopropanol cleaning in an ultrasonic bath, a layer of AZ 5214 E resist is placed on the niobium film. The spin coater used for this process leaves a wall of coating at the edges of the chip, the so call edge bead [Fig. 3.1(b)]. To prevent a ring of untouched niobium at the edges due to this wall, the edge bead has to be removed separately. Using optical lithography, the coating is exposed to ultraviolet light through a mask which contains a structure that exposes only the edge bead [Fig. 3.1(c)]. This step is done in the Carl Süss mask aligner MJB 3. With the help of the developer AZ 726 MIF the exposed parts of the coating are dissolved [Fig. 3.1(d)]. The optical lithography step is then repeated using a mask that contains the actual structure, leaving coating in form of the structure [Fig. 3.1(e),(f)]. The edge bead removal step is also necessary to ensure that the mask is in contact with the resist during the exposure step to provide optimal sharpness in the second step. The chip is then processed in a PlasmaLAB 80Plus reactive ion etcher by Oxford where a SF_6 and argon plasma is shot at the chip. The plasma leaves the niobium protected by the coating and etches the unprotected niobium away,

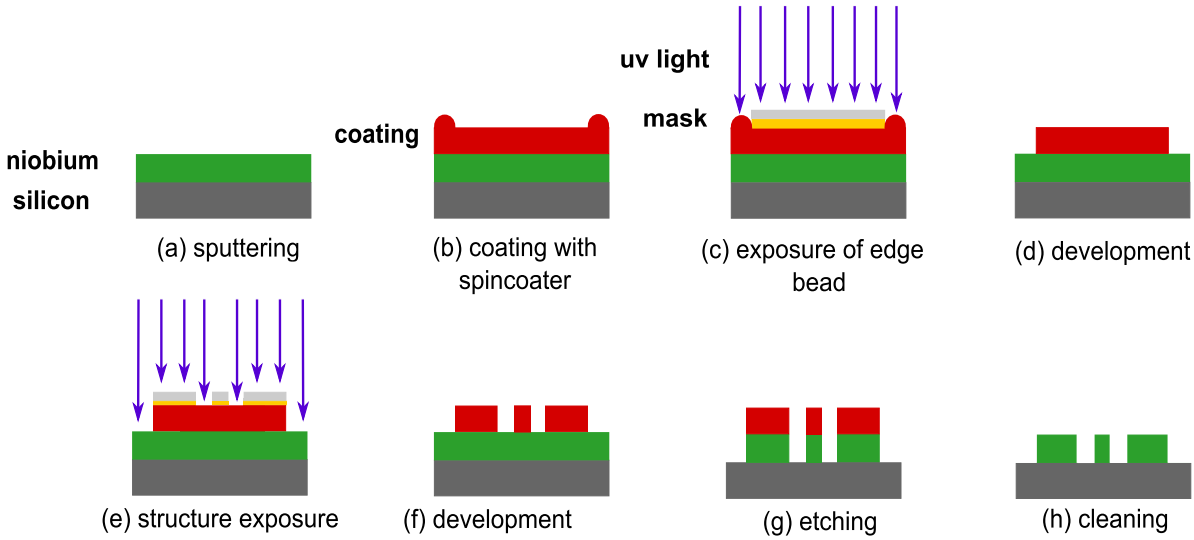

Figure 3.1: The fabrication steps of microwave chips produced with optical lithography.

transferring the final structure to the niobium film [Fig. 3.1(g)]. After resist stripping in an additional cleaning step, the chip is ready for measurement [Fig. 3.1(h)]. A table with the design parameters for the structures investigated in this thesis can be find in App. A.

3.2. Setup for cryogenic transmission measurements

The measurement of superconducting devices in a broad frequency range can be very demanding. Every impedance mismatch in a feed line or output line can result in parasitic resonant structures in the frequency dependent transmission measurement. Therefore, it is very important to ensure an experimental setup with as few reflection planes as possible as well as to reduce impedance mismatches at each plane. The measurements described are carried out in a liquid-^{4}He-cryostat, that was optimized for these kind of measurements in the course of this thesis. Other key parts, that need to be optimized to allow for exact measurements, are the feed and output lines, the sample box including the printed circuit board (PCB) in which the sample is mounted and the connection from PCB to the sample.

3.2.1. Liquid-^{4}He-cryostat

In Fig. 3.2, a sketch of the liquid-^{4}He-cryostat is shown. The sample box, which contains the chip, lies in a liquid helium environment, which cools the sample to 4.2 K. The helium bath is thermally shielded from the outside by an evacuated dewar. The box is connected to the outside of the cryostat by a set of minibend cables, followed by stainless steel cables. The latter are connected to a vector network analyzer by flexible microwave cables. The different cables are connected to each other by feed through adapters, which serve the purpose of hermetic sealing and increasing the mechanical stability. The latter is especially required for SMP connectors whose performance is degraded when too large bending forces act on the connector interface. We minimize the number of reflection planes by avoiding additional adapters between different connector series and instead make use of cables with different connectors at each end. Prior to this work, the liquid-^{4}He-cryostat has been equipped with a set of astro-cobra-flex cables (31086S) and two stainless steel cables. While the cobra cables have low loss, their impedance is poorly matched to the input line [see Fig. 3.3] and to the lines leading to the sample, whose impedance is close to 50 Ω. In the measurements performed in this thesis, additional loss does not add any disadvantages as long as the power level does not become too low. The use of stainless steal cables adds a loss of approximately 10 dB to 20 dB depending on frequency. Additional loss has the positive side effect, that outgoing signals that are reflected inside or at the end of the cables are dampened two times by the cables, which ensures that they are small in comparison to the input signal when they re-enter the chip. In Fig. 3.3 a TDR measurement of the impedance of a stainless steel cable is shown in comparison to one of a cobra-flex cable. In TDR measurements a step pulse is sent through the device under test and the time dependent reflection is measured. This can be converted to a spatial or time dependence of the impedance. The slope of impedance stems from the fact that high loss is detected as an impedance mismatch and is not a real feature of the impedance of the cables. Bends in the cable lead to a change in distance between the inner and outer conductor and therefore can change the impedance. The stainless steel cables are bent two times, which is necessary because of possible contractions when cooling down the cryostat. These two bends can be seen in the measurement at 58.5 ns and 60.2 ns. In addition to the bad matching of the cobra cables, they also show multiple impedance mismatches and an overall rougher behaviour. The test signal reaches the end of the cobra cable at approximately 60 ns, which is indicated by the sharp change in impedance and the rise to very high impedance values. The transmission measurement [Fig. 3.4] through two stainless steel cables shows

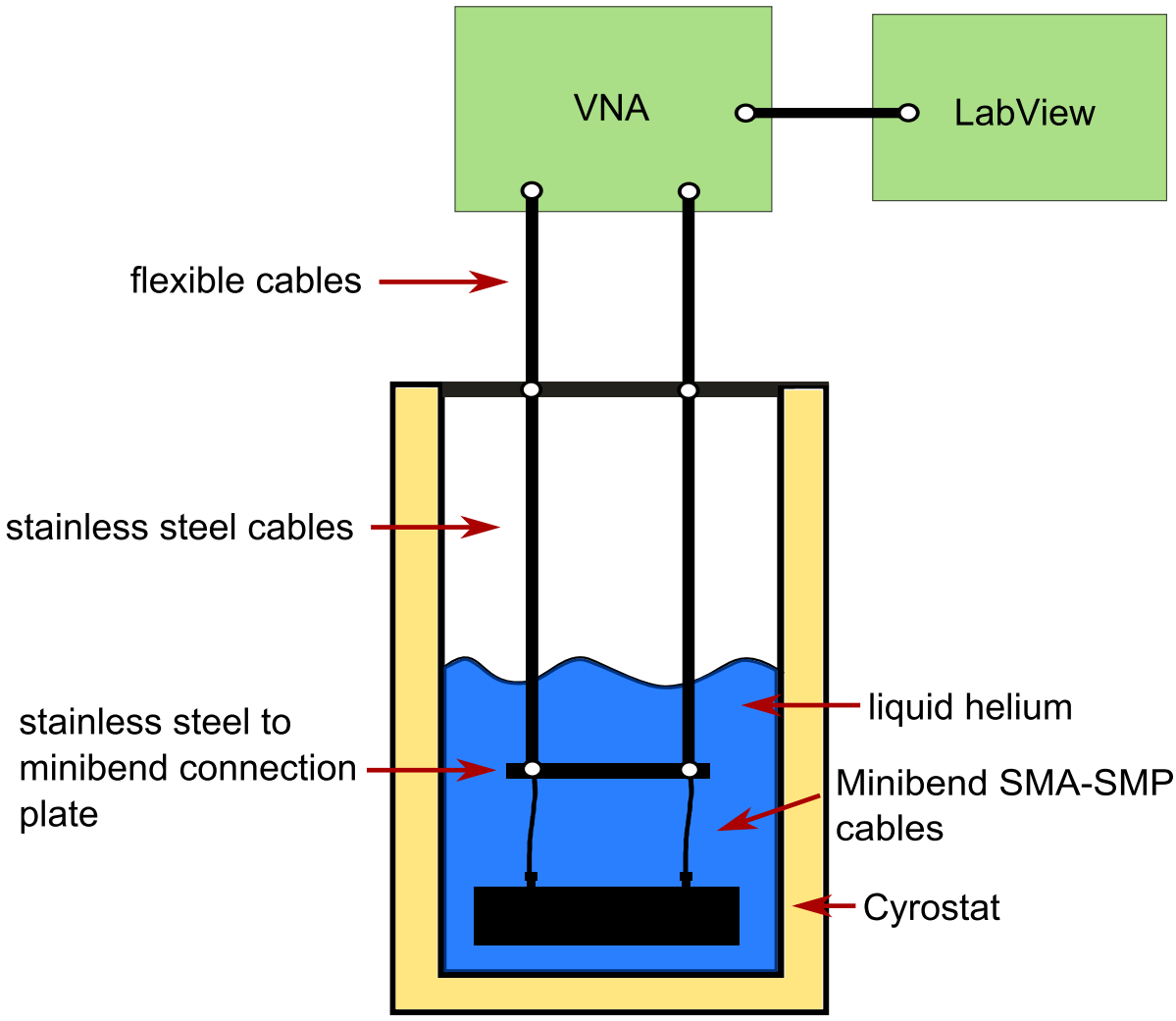

Figure 3.2: A sketch of the liquid-^{4}He-cryostat.

a downwards slope due to the frequency dependent loss of the cables. The transmission is very smooth until a frequency of approximately 11 GHz where small oscillations can be seen. These oscillations are far away from the working point of the measured devices and therefore do not influence our measurements. At the planned working frequency of 5.75 GHz of most of the devices in this thesis, the loss per cable is -8 dB, which does not affect the measurements negatively. The measurement is first performed with the two cables connected with two 90° pieces and an adapter and afterwards connected with a minibend cable. The line including a minibend cable exhibit a higher loss than the one with a combination of 90° pieces, but has a smoother behaviour above 11 GHz compared to the case with 90° adapters.

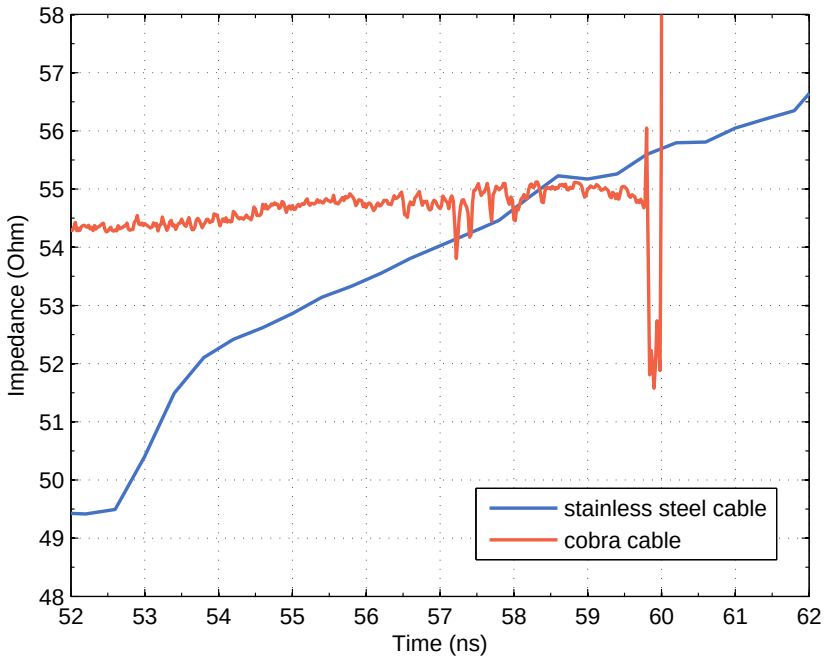

Figure 3.3: TDR measurement of a stainless steel cable now used inside the cryostat (blue line) and an old cobra cable which is now removed (red).

3.2.2. Sample box

For the measurement, the sample is fixed in a sample box made of copper [see Fig. 3.5]. The box consists of a ground, a cover and a lid. The lid has eight holes in it to connect the SMP connectors on the PCB [see also Sec. 3.2.3]. The cover is used to allow only a small mode volume above the PCB to avoid additional unwanted modes, which could lead to reduction in transmission or reflection due to loss or interference effects. It also provides a better isolation between the different transmission lines of the PCB.

3.2.3. Printed circuit board

To allow for multiple, in this case eight, connectors to be used with the only 12 mm × 12 mm big chip, the chip is placed into a printed circuit board (PCB). The PCB is a 635 µm thick plate made of Rogers 3010, a dielectric with a similar relative dielectric constant to that of silicon. The dielectric is coated with 35 µm of copper on both sides. One side has been etched to contain transmission line structures, that lead from the central chip

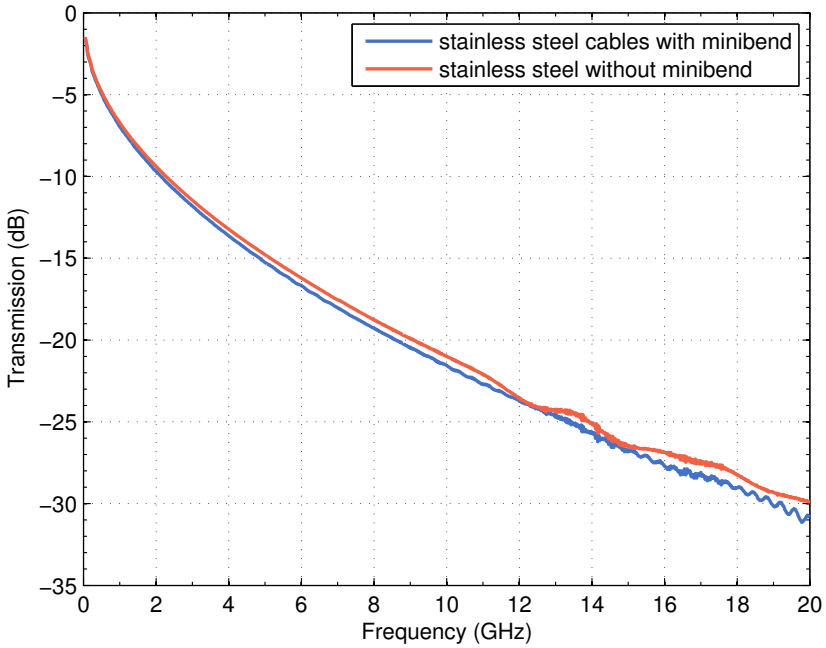

Figure 3.4: A transmission measurement through two stainless steel cables, connected with two 90° adapters (red, without minibend) and with a minibend cable (blue).

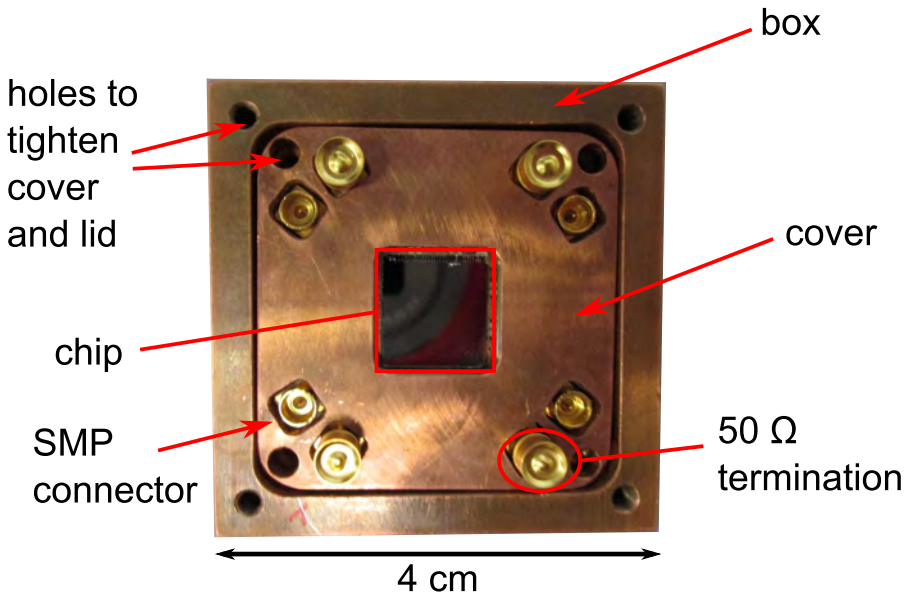

Figure 3.5: A picture of a sample box with chip, cover and 50 Ω terminations.

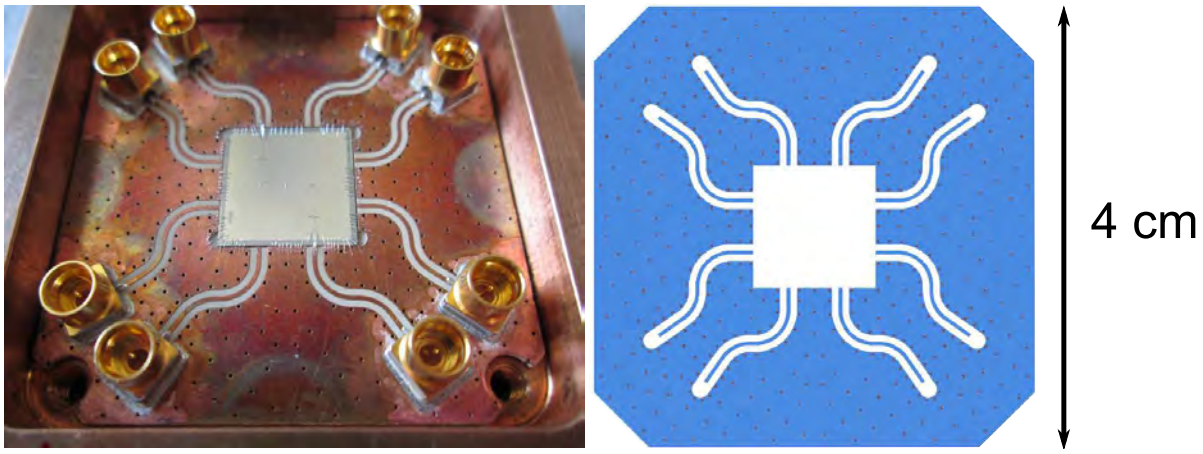

Figure 3.6: Picture of PCB in a sample box with a contacted calibration chip inside (left panel) and its model (right panel).

to the surrounding connectors. The design for the PCB used in this thesis is shown in Fig. 3.6 next to a picture of the chip placed in the PCB and box as it is used in measurements. As can be seen in the picture, the PCB has also holes in it, that are coated with copper. These so called vias are used to connect the bottom plane on the backside of the PCB to the CPW ground planes of the top plane. This leads to a consistent potential of all parts except the inner conductor. This is needed, so no waves can be build between the front and back ground plane of the PCB and also suppresses slotline modes in the transmission line. To understand the importance of vias in the PCB see the simulation discussed in Sec. 4.1.1.

The connectors on the PCB are SMP connectors (19S102-40ML5) produced by Rosenberger. They are soldered to the board with soldering paste in a special oven for soldering electronics at the Physik Departement of the Technische Universität München. The oven is a gas phase oven in which the different parts are evenly heated independent of their material type. After applying the soldering paste with a stencil [see Fig. 3.7(a)] and carefully placing the connectors in the right position with the help of a mask [Fig. 3.7(b)], the PCB is put in the oven and heated above the needed temperature for soldering. Since the quality of the connection between inner conductor of the board and the pin of the connector increases with small pressure on the pin, these connections are soldered manually. Solder flux and small solder plates are placed below the pin, which is then heated using a soldering tool, while applying light pressure on the pin. With this technique a good consistency and good impedance mismatch values of the board-connector transition of around $6\,\Omega$ can be achieved.

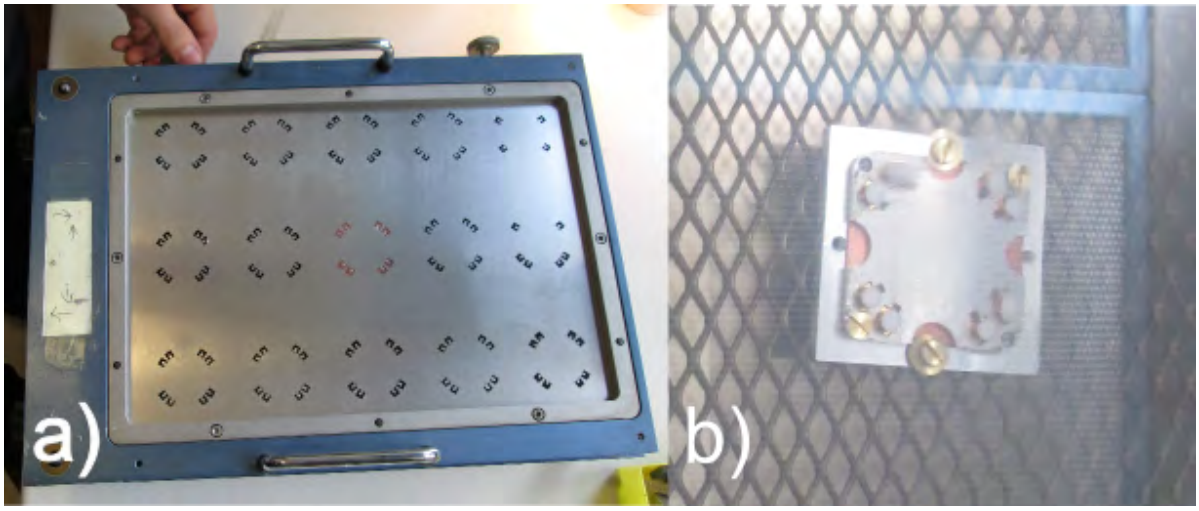

Figure 3.7: Pictures of the soldering stencil (a), and the PCBs with aligned connectors in the oven (b).

3.2.4. Bonding

As seen in Fig. 3.6, the chip is put inside a pocket in the PCB and then connected with aluminium bonds. The bonds are not superconducting in the 4.2 K measurements, as the critical temperature for aluminium is 1.14 K. Aluminium bonds are known to have bad performance above approximately 10 GHz [21], but since the working frequencies of the devices measured in this thesis are around 6 GHz, this is believed to be no limiting factor for the measurements. The inner conductors of PCB and chip are connected with five bonds each, the ground planes with approximately 100 bonds. It has been shown, that especially the number of bonds on the inner conductor improves the impedance matching of the transition which leads to better performance of the device under test [22]. The inner conductors of the unused lines on the PCB are each shorted to the outer conductor at the chip to prevent them from acting as resonators. In addition, a set of bonds is put on the chip from one outer conductor to the other, over the inner conductor and gaps, to ensure an equal potential of the outer conductors to suppress slotline modes.

3.2.5. Calibration

To account for contributions of the surrounding setup, such as the loss of the cables or impedance mismatches at the transition from one cable to another, a calibration is

needed. In order to imply as many parts of the setup as possible, the calibration is performed with a calibration chip. The design of the chips used in the calibrations are shown in Fig. 3.8. The calibration chip is installed in the same way as the devices to be characterized. A transmission measurement is then performed and the result is used to calibrate the following measurements. A problem with this technique is, that parasitic features of the calibration chips are also included in the calibration itself, meaning that a resonance that occurs on the calibration chip will show up as peaks in the actual measurement. In order to achieve a calibration that does not lead to such features, it is important to ensure a smooth transmission through the chip. Simulations show that the chip design should indeed lead to a smooth transmission [see Sec. 4.2]. The transmission measurement of such a calibration chip [Fig. 3.9] also shows a smooth behaviour up to a frequency of 4 GHz, but is then interrupted by dips.

Since all the measurements done so far do not use all of the eight input lines on the PCB, it is important to terminate these lines with 50 Ω loads. The loads are installed directly on the SMP connectors. Figure 3.9 presents a comparison of a measurement of a calibration chip with and without termination of unused ports. The parasitic dips are suppressed by the terminations, which leads to a much better transmission. The drop in transmission with frequency seen in the measurement stems mainly from the frequency dependent loss of the stainless steel cables.

The improvements that the different cables, new SMP connectors, new sample box and cover create, can already be seen in the calibration measurements. In Fig. 3.10 a comparison between a measurement with the old setup (used in [22]) and the new setup is shown. The measurement in the new setup proves to be smoother, especially at the frequencies of interest around 5.75 GHz.

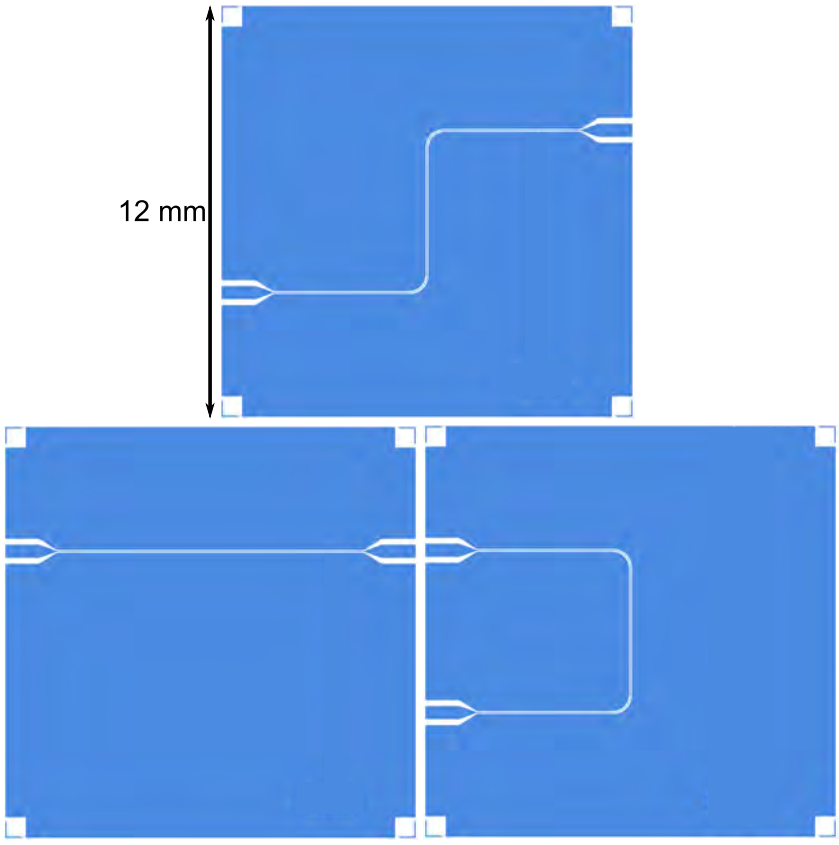

Figure 3.8: Design for the calibration chips. They are used for straight (bottom left), diagonal (top) and isolation (bottom right) calibrations. All lines are design to have an impedance of 50 Ω.

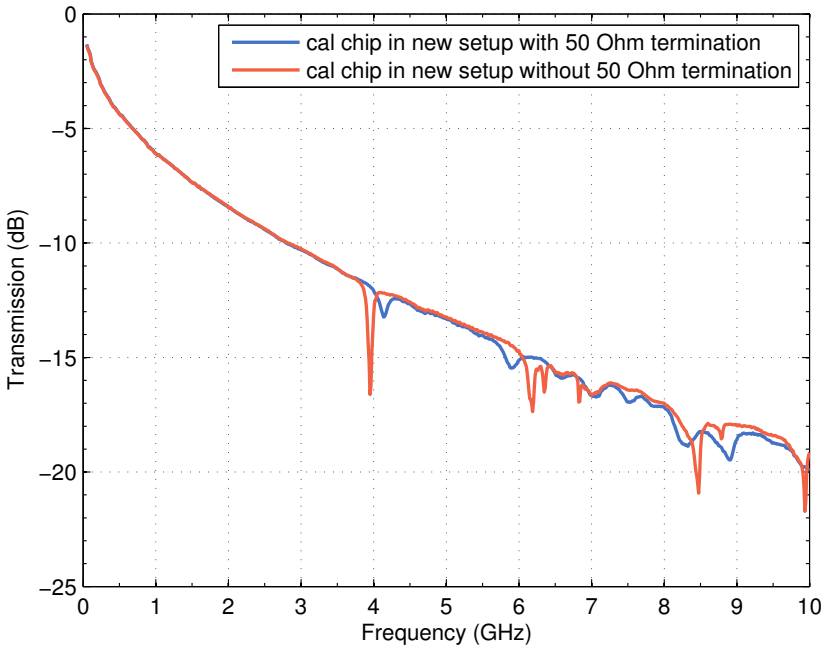

Figure 3.9: Comparison of calibration chip measurements of a chip with 50 Ω termination on the unused SMP connectors on the PCB and of a chip without the terminations.

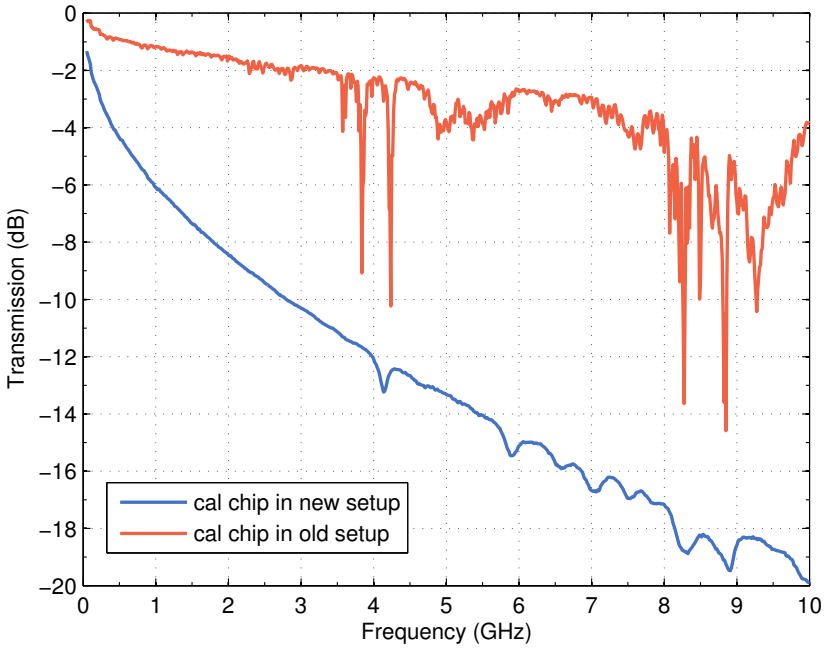

Figure 3.10: Measurement of a calibration chip in the old setup, using cobra cables, mini-SMP connectors and an old version of the sample box [22], and a measurement in the new setup described in this chapter.

4. Simulations

In microwave technology, simulations are a strong tool to predict the properties of devices. In general, simulations reduce the number of prototypes, cut costs and accelerate the design phase. More specifically, features stemming from the actual device can be separated from features that appear only in the measurement which is an indication that they are related to the electromagnetic environment or the experimental setup. In order to improve our designs and to find flaws in the measurement setup, we perform substantial simulations of PCBs, beam splitters and interferometers as part of this thesis. The simulations are performed with CST microwave studio [19].

4.1. Simulations of PCBs

As mentioned in Sec. 3.2.3, the design of the PCB and the connectors on the PCB is very important for the measurement, as it is very easy to produce impedance mismatches by small misalignments of the connectors or disturbances in the CPW mode of the transmission lines by misplaced vias. To show the importance of the latter, the next part focuses on simulations concerning the placement of vias.

4.1.1. The importance of via placement

To check the performance of the PCBs a board with continuous transmission lines at the chip site, shown in Fig. 4.1, is linked with SMP connectors and measured with a ZVA 24 vector network analyzer from Rohde & Schwarz. Just like in the cryostat, minibend cables are used to connect the PCB with the measurement cables. In this measurement the cables leading to the ZVA are calibrated, so that the measured transmission shows the properties of the system consisting of the PCB and two minibend cables. The measurement [Fig. 4.2] shows a large dip of $-12.7\,\mathrm{dB}$ at $12.0\,\mathrm{GHz}$ that is not expected when

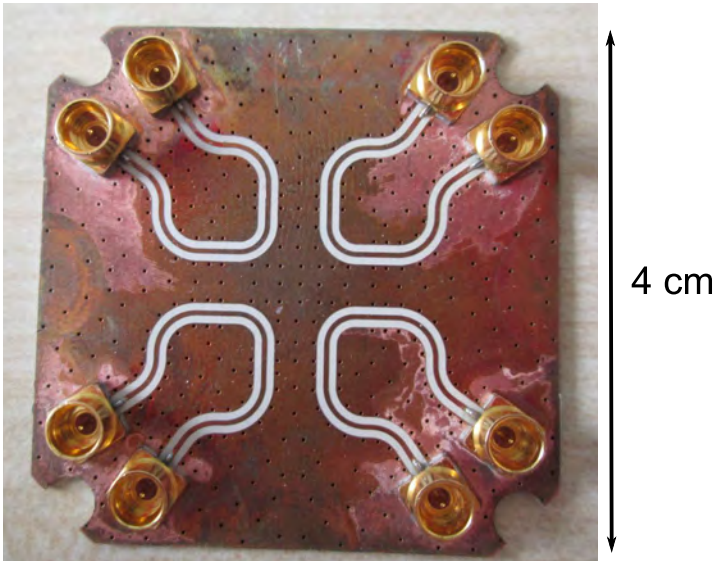

Figure 4.1: Picture of the measured and simulated PCB.

considering the PCB at a first glance [see Fig. 4.1]. The simulation of this PCB also shows a dip at nearly the same frequency of 11.9 GHz [Fig. 4.2]. The model used for the simulation is shown in the left panel of Fig. 4.3. Taking a look at the electric field on top of the PCB [see left panel in Fig. 4.4] and on a cutting plane through the curve [right panel of Fig. 4.4] at the dip frequency, we observe, that at the middle of the curve, the field is no longer a CPW mode. Furthermore, the field leaks out of the transmission line to build a standing wave in the whole PCB substrate, which also excites other transmission lines. We note, that the field anomaly occurs in a region where the via density is quite low although the bend of the CPW is pronounced. In order to judge if this is the reason for the formation of the parasitic mode, we simulate a design with more vias in the problematic region which is displayed in the right panel of Fig. 4.3. The simulation shows that with an increased via density at the critical curve, the dip in transmission vanishes [see Fig. 4.2]. Thus, the simulation allows us to determine the origin of the parasitic dip. We come to the conclusion that the via placement and density in curves are crucial for the performance of CPW devices.

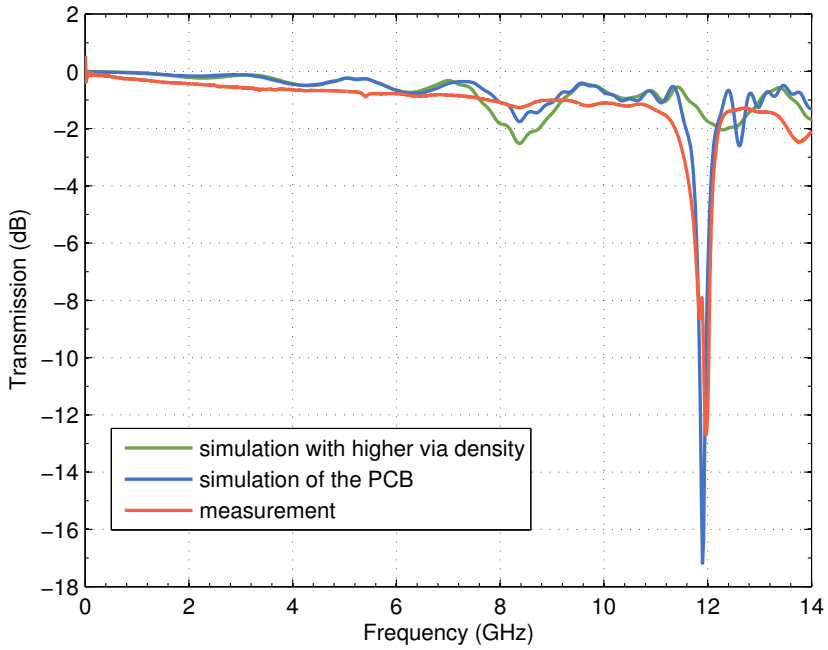

Figure 4.2: Comparison of simulated and measured transmission. The measured transmission of the board depicted in Fig. 4.1 shows a pronounced dip (red curve). The corresponding simulation reproduces the dip very well (blue curve), whereas the dip is suppressed in a simulation with a higher via density (green curve).

4.1.2. Performance of the transition between Rosenberger connectors and the PCB

Previous to this work, Mini-SMP connectors were used to connect the transmission lines on the PCB to feed lines and outgoing lines. Since they have proved to have a high impedance mismatch at the transition to the PCB, they are replaced with SMP connectors. With a simulation of two SMP connectors on a small PCB [see Fig. 4.5], we evaluate the performance of the used connectors. The PCB contains a straight transmission line from one connector to the other. Parts of the connectors are filled with a dielectric similar to the one used in the connectors of the minibend cables to ensure a good matching at the top of the connectors. The ports are placed on top of said dielectric. In order to simplify the simulation model, the solder joint is represented by a cuboid made of copper. The simulations show that the connectors feature very little reflection of $-20\,\mathrm{dB}$ and below for frequencies up to $8\,\mathrm{GHz}$ [see Fig. 4.6]. The transmission loss through the connectors and PCB is dominated by the loss of the PCB and the additional dielectrics in the connector and is very smooth up to a frequency of $8\,\mathrm{GHz}$. To conclude,

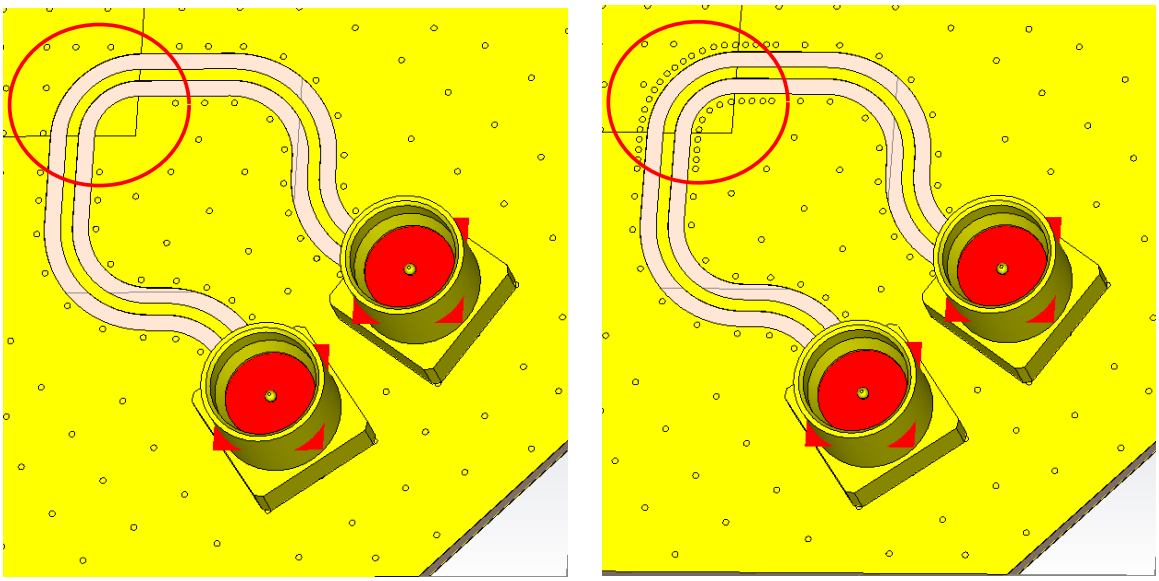

Figure 4.3: The two models used for analyzing the effects of vias. Left panel: Model corresponding to the measured PCB. Right panel: Model with an increased via density at the curve marked by the red circle.

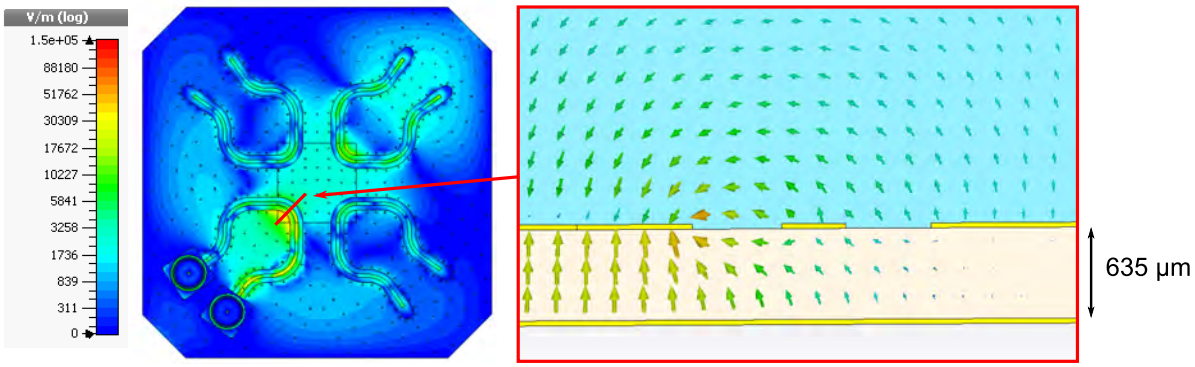

Figure 4.4: Simulation results. Left panel: absolute value of the electric field (color code) at the surface of the PCB. Right panel: electric field (arrows) at a cut through the PCB marked by the red line in the left panel.

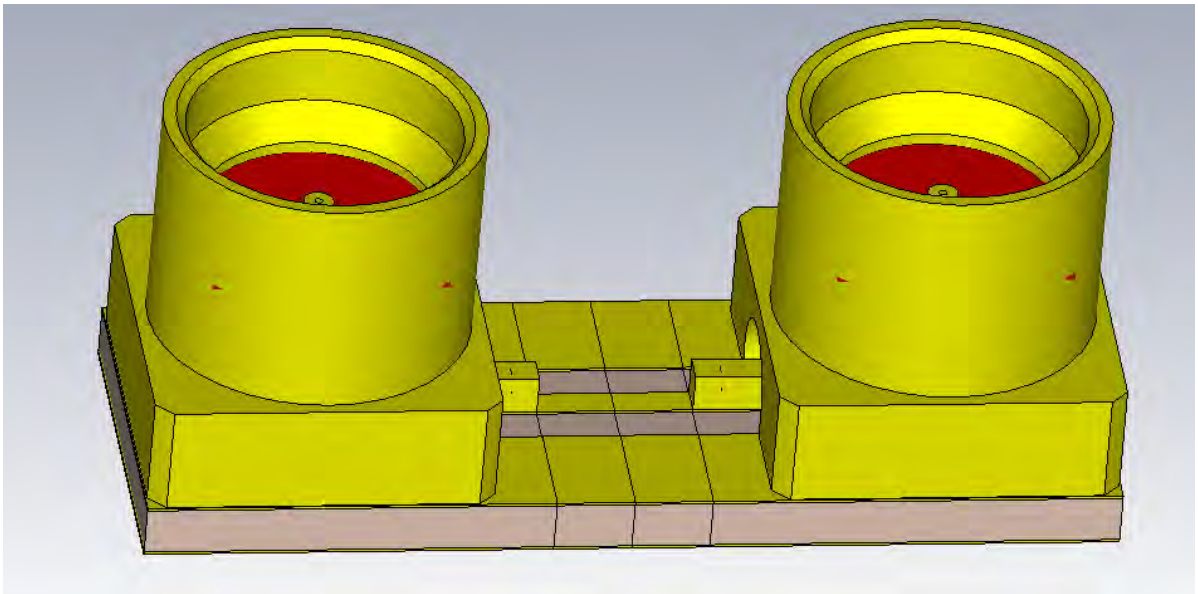

Figure 4.5: Picture of the model used to simulate the performance of Rosenberger SMP connectors.

the low reflection of the connectors is very promising for transmission measurements with SMP connectors. However, the simulation provides the results for a perfect transition between connector and PCB and does not account for connector misplacement or solder paste under the connector. Therefore, it is important to optimize the soldering process to avoid additional reflections [see Sec. 3.2.3].

4.1.3. Simulation of a PCB without a chip site

In Sec. 4.1.1, we showed the importance of vias by simulating a PCB with an imperfect distribution of vias. The PCBs used to connect the chips in the measurements do not contain the critical curve of the latter simulation as it lies in the recess for the chip. In order to see whether the via placement of the actual boards lead to similar problems, a simulation of a model with a straight connection at the chip site is performed [see Fig. 4.7]. The connection is equipped with the same via density as the rest of the transmission lines and should not lead to reflections. Therefore, the simulation shows the properties of the parts leading from the connectors to the chip. The simulated transmission is very smooth [see Fig. 4.8]. The slope in transmission stems mainly from the loss of the PCB. In comparison to the simulation, the measured transmission through a similar board has more loss and is overlaid with an oscillation that is not seen in the

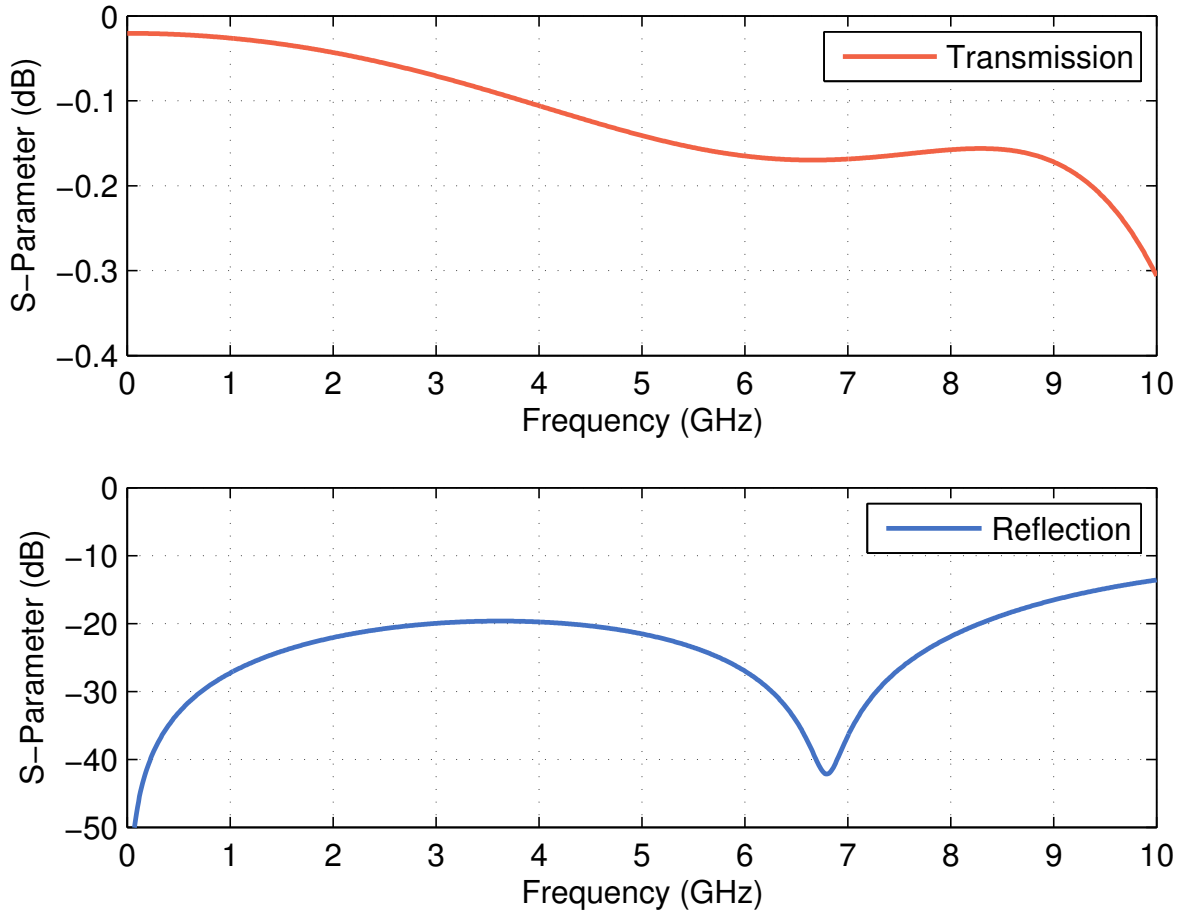

Figure 4.6: Results of the simulation of two SMP connectors on a small PCB. The system shows a transmission with low loss and smooth behaviour up to 6 GHz (top panel) and low reflection (bottom panel).

simulation. The measurement is performed using minibend cables, that connect the board to the measurement cables. The minibend cables are not included in the calibration of the measurement cables, which leads to additional loss. The oscillations seen in the measurement might stem from the higher impedance mismatch at the transitions between board and connectors compared to the simulation and from the additional reflection planes due to the minibend cables. The simulation shows that the boards with a recess for the chip are suitable for transmission measurements of microwave devices at least up to a frequency of 10 GHz. The via placement at the transmission line between connector and chip leads to a smooth behaviour of the board.

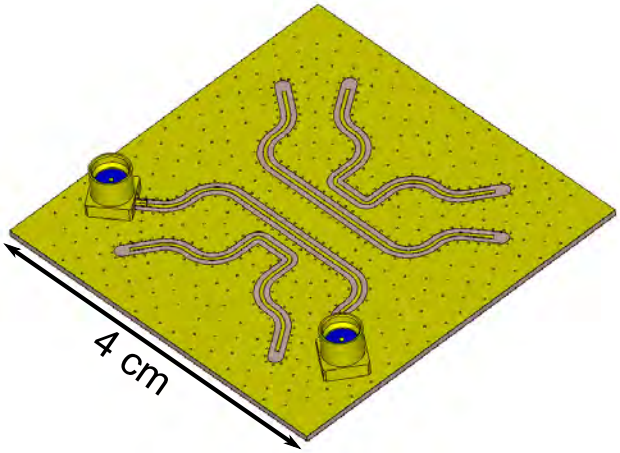

Figure 4.7: Model of a PCB without a chip site.

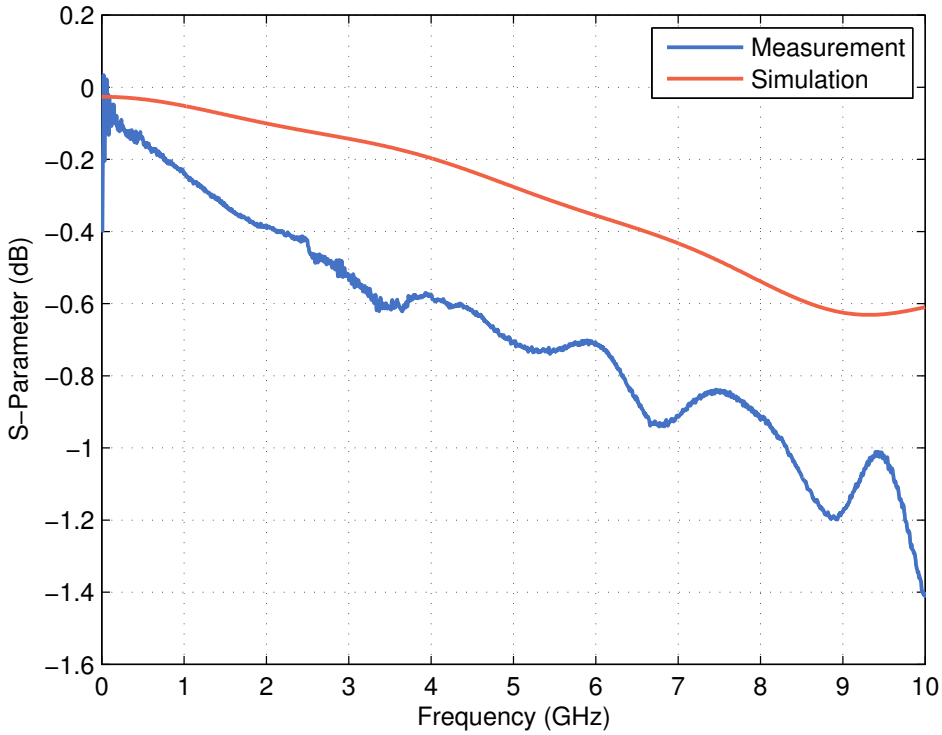

Figure 4.8: Results of the simulation of a PCB without a chip site in comparison to the measurement results of the same board.

4.2. Simulation of calibration chips

In Sec. 3.2.5, we show that the chips used for calibration of the transmission measurements of microchips show dips in the transmission, that are difficult to be explained by the structure of the chip. In order to better understand the behaviour of the calibration chips, we perform a simulation of the latter. The model for the simulation consists of a 250 µm thick silicon chip with a 100 nm thick perfectly conducting layer on top of it [see Fig. 4.9]. The niobium used in the experiments is replaced by a perfectly conducting layer to improve the performance and speed of the simulation.

The chip is structured with a transmission line used for straight calibrations [see Fig. 3.8] with no niobium at the edges to include the effects of the edge bead removal. Below the silicon wafer there is a 385 µm thick Rogers 3010 layer. In contrast to the measurements, the simulated transmission through the calibration chip has a smooth behaviour up to a frequency of approximately 11 GHz [Fig. 4.10]. The measurement shows multiple parasitic resonances starting at a frequency of 4 GHz [see Fig. 3.9]. However, in the simulation, we can see a first distinct dip of 1.6 dB depth at 11.7 GHz in the transmission through the calibration chip. To better understand this behaviour, the electric field is simulated for different frequencies [see Fig. 4.11]. At 1.0 GHz, where the transmission through the chip is almost perfect, the electric field is concentrated in the transmission line and a small area around it, with no additional parasitic modes or resonances on the chip. There is still a high concentration of electric field around the transmission line at 11.7 GHz, the frequency of the dip in transmission, but we also observe a dominant parasitic field mode in the substrate of the chip. Looking at the backside of the chip [Fig. 4.11 (bottom panel)], it is clear, that the mode is a higher order mode. In the simulation of the calibration chip, two lower order modes can be seen at 6.0 and 8.0 GHz, but compared to the one at 11.7 GHz the dips in transmission are rather small. The lower order modes seem to be suppressed by the geometry of the calibration chip, as they are more dominant in simulations of other microwave chips [see Sec. 4.3].

The behaviour of the measured calibration chip [see Fig. 3.10] can currently not be explained by the simulation, as the structures in the measurement differ from the ones seen in the simulation. In addition, the depth of the dips change with the implementation of 50 Ω loads as shown in Sec. 3.2.5. This leads to the conclusion, that the dips seen in

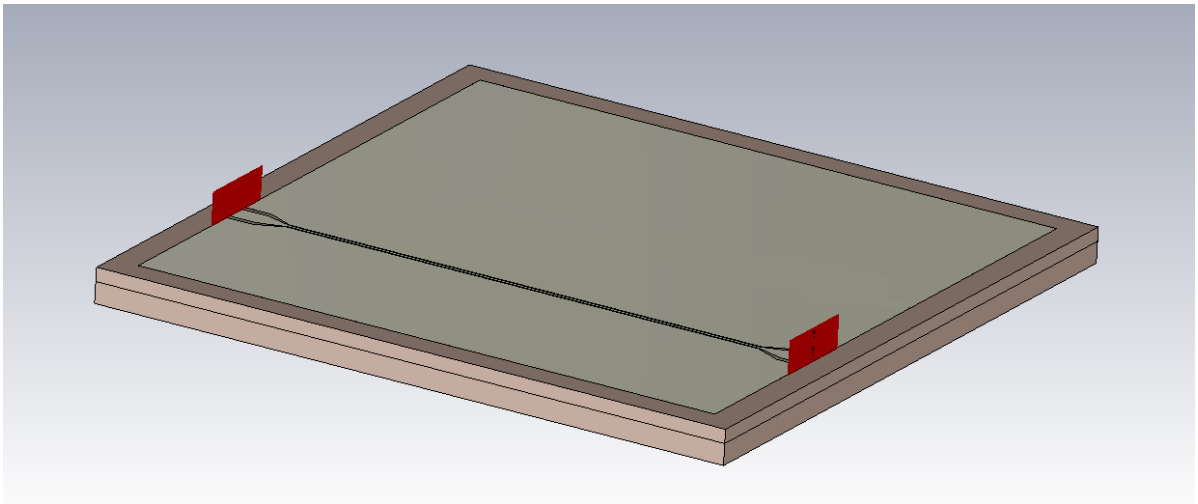

Figure 4.9: Model of a calibration chip.

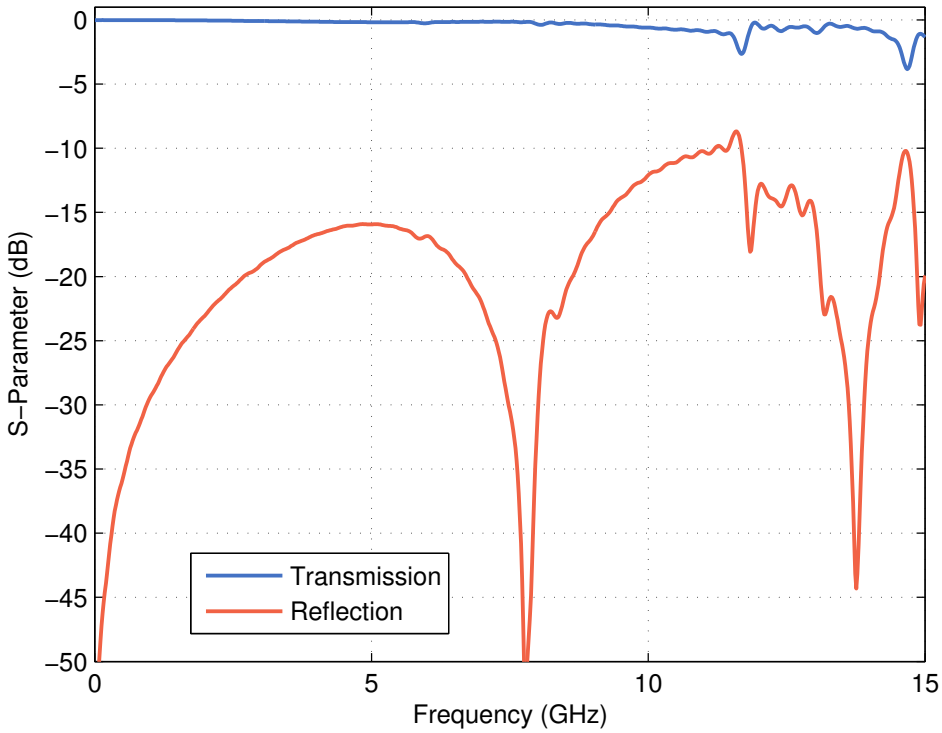

Figure 4.10: Simulation results of a calibration chip.

the measurement likely stem from the surroundings, most likely the unused transmission lines of the PCBs, or from reflections at the bonds.

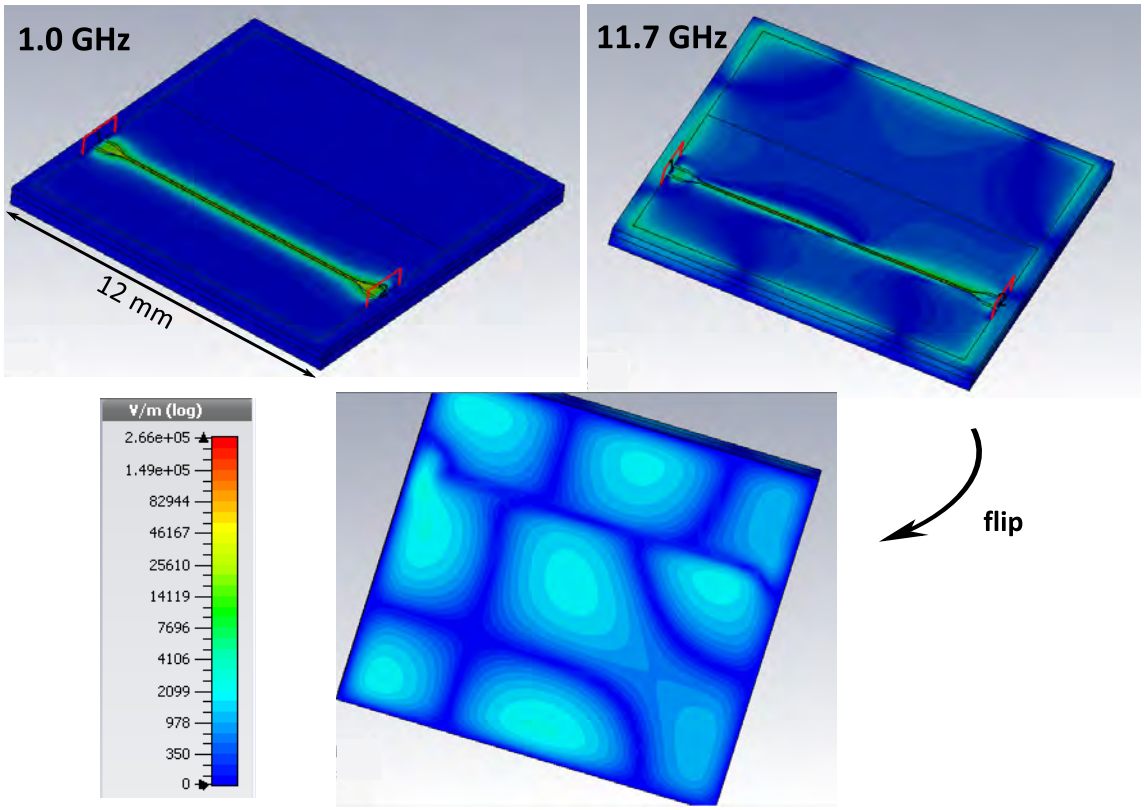

Figure 4.11: Modes of the calibration chip at 1.0 GHz and 11.7 GHz.

4.3. Simulations of beam splitter designs

There are many different ways to implement on-chip beam splitters with transmission lines. Therefore, it is important to have a way to predict the performance of the built devices. By simulating different designs of beam splitters, we can compare the results and choose the best design for our purposes and implement changes, that lead to an improved behaviour of the devices. In this section, we show the simulation results of two different beam splitter designs, that are measured in the master's thesis of Christian Schneider [23].

4.3.1. Beam splitter with straight arms

The first design examined in this thesis is one of the most simple designs, where the arms of the beam splitter are straight transmission lines [see Fig. 4.12]. It is advantageous since it minimizes the amount of curves needed in the beam splitter, which leads to

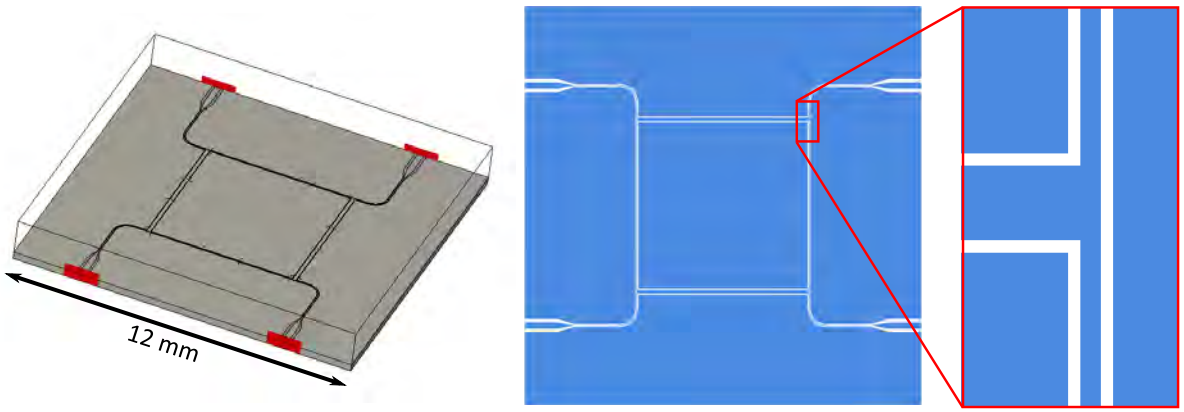

Figure 4.12: Model of the straight beam splitter used for the simulation (left panel) and a sketch of the structure from the top (middle panel) with a zoom on the junction of the beam splitter (right panel).

fewer critical points. This makes it bigger in size compared to other designs which is impractical for combining it with other devices. The simulation model includes a silicon substrate and a perfectly conducting layer. Bonds connect the ground planes of the CPW transmission lines. The designed working frequency f_{work} is 5.75 GHz. The simulation shows a working frequency of 5.83 GHz with a transmission of −2.75 dB and −3.35 dB at the straight and cross transmission, respectively [Fig. 4.13]. The isolation is −25.6 dB. At approximately 7.6 GHz, we observe a resonant structure in all three transmissions. By looking at the simulation of the electric field of the system [Fig. 4.14], we observe that the structure at 7.6 GHz originates from a resonant mode in the substrate of the chip, probably a lower order mode of the one discussed in Sec. 4.2. If we compare the simulation results with the theory of a beam splitter, introduced in Sec. 2.3, we observe, that the cross transmission is lower and the straight transmission is higher than expected for the working frequency. The theoretical calculations predict similar behaviour for impedance deviations from the design values in the arms of the beam splitter, which could be the reason for the properties of the measurement. This cross over between the two transmission ports can also be seen in measurements of a similar design [23]. Apart from the disparity at the working frequency and the previously discussed feature at 7.6 GHz, the simulation of the beam splitter predicts scattering parameters similar to the theory without impedance mismatches. Especially the cross transmission follows the theory very closely.

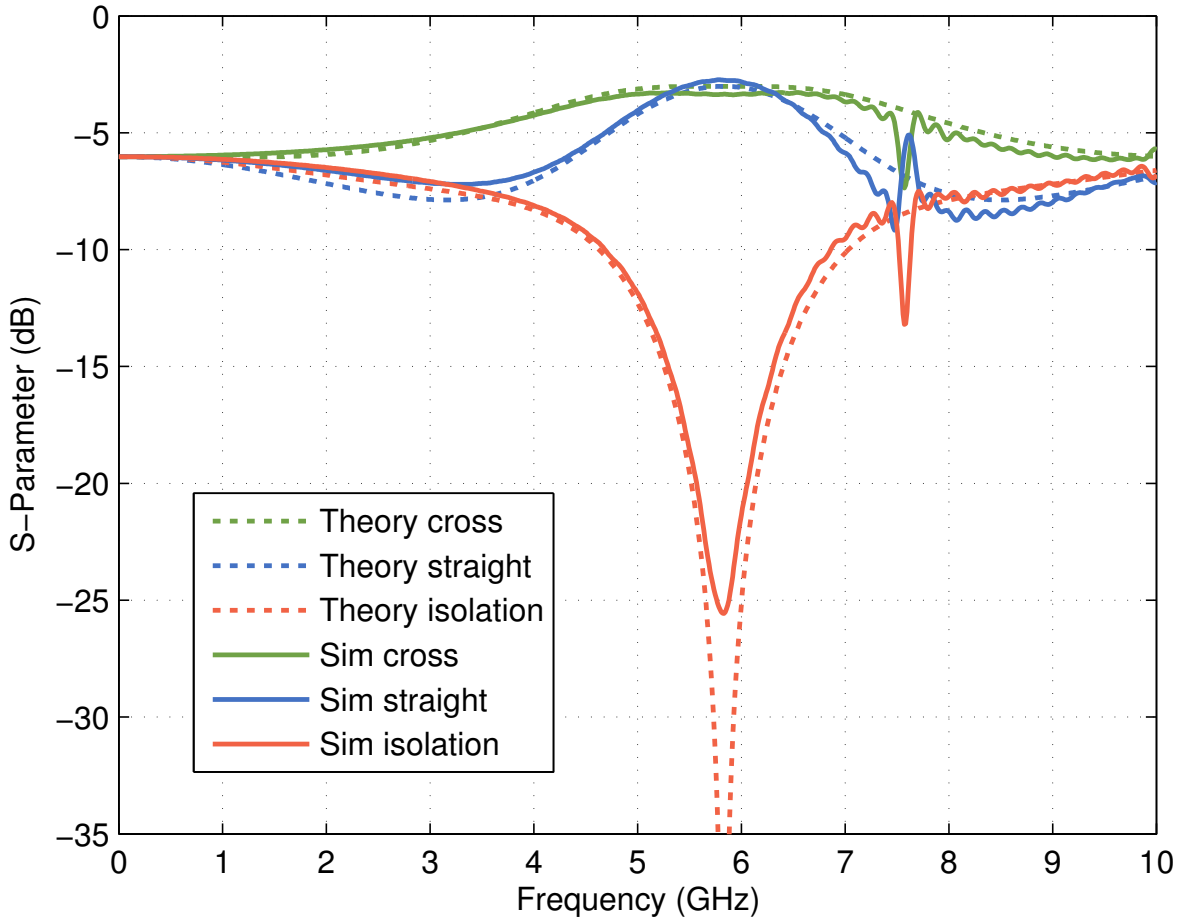

Figure 4.13: Results of the simulation of the beam splitter shown in Fig. 4.12 (continuous lines) in comparison to the theory of a beam splitter (dashed lines).

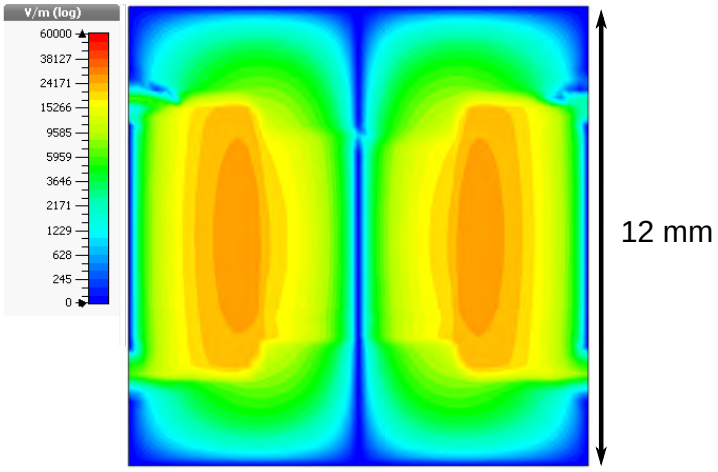

Figure 4.14: Simulation of the electric field at the backside of the straight beam splitter at 7.6 GHz.

4.3.2. Beam splitter with meandered arms

The second design examined has been created to decrease the size of the beam splitter. For applications, such as the interferometer, the beam splitters needs to be of smaller size in order to fit the entire device on a $12 \times 12\,\mathrm{mm}$ chip. Therefore, two arms of the beam splitter across from each other are meandered to save space [see Fig. 4.15]. It is important to choose the radius of the curves large enough, so that the crosstalk between different parts of the transmission line is minimized and slotline modes are not excited. The design rule used for the radius is

$$\mathrm{r_{curve}} \geq 5 \cdot W, \tag{4.1}$$

where W is the width of the inner conductor of the CPW. The beam splitter is designed for a working frequency of 5.75 GHz. In the simulation the working frequency is shifted to 5.56 GHz, approximately 0.2 GHz below the design value [see Fig. 4.16]. With an isolation of $-29.8\,\mathrm{dB}$ the meandered beam splitter outperforms the isolation of the straight one by almost 5 dB. If we account for the small shift in working frequency, the simulation of the S-parameters of the cross and straight port follow the theory very closely. At the working frequency the simulation predicts a transmission of $-3.05\,\mathrm{dB}$ and $-3.01\,\mathrm{dB}$ at the straight and cross port, respectively [see Fig. 4.17]. The small deviation from the theory stems from an oscillation, that is caused by a parasitic mode at 4.8 GHz. This could be an effect of the Fourier transformation used by the time domain solver of the simulation software used for the simulation of the beam splitters. Looking at the electric field at this frequency, we can assign the feature to a mode in the substrate of the chip [see Fig. 4.18]. The observed mode appears to be the ground mode of the ones seen at higher frequencies, with the nearest to the working frequency being at 6.6 GHz. The latter is similar in shape to the one observed in the simulation of the straight beam splitter, but is shifted by approximately 1 GHz. At the working frequency, the imbalance of the cross and straight S-parameters of 0.6 dB, observed in the simulation of the straight beam splitter, has almost vanished. But a disadvantage of the meandered beam splitter is, that there appears an additional mode in the substrate at 4.8 GHz and the higher order modes are shifted to lower frequencies, which brings them nearer to the working frequency. Nonetheless, the meandered beam splitter shows better behaviour around $\mathrm{f_{work}}$ than the straight beam splitter.

As can be seen in Fig. 4.19, the simulation of the meandered beam splitter describes

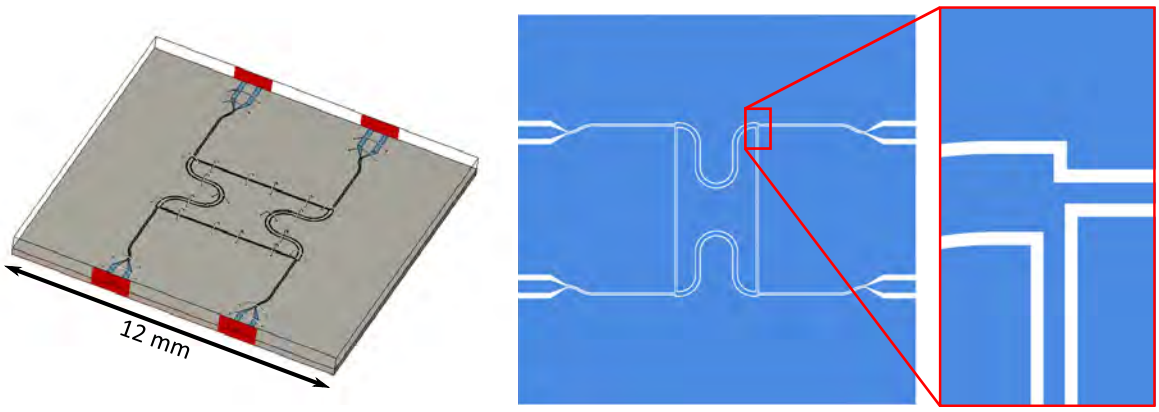

Figure 4.15: Model of the meandered beam splitter used for the simulation (left panel) and a sketch of the structure from the top (middle panel) with a zoom on the junction of the beam splitter (right panel).

the measurement of the according chip quite well. The measurement was performed by Christian Schneider and a more detailed description can be found in Ref. [23]. For frequencies of up to 4 GHz the measured S-parameters are lower than the simulation, but follow the same tendency. In this frequency range, the measurement is overlayed by an oscillation, which possibly stems from the measurement setup. The first chip mode, predicted at 4.8 GHz, is observed more dominant than in the simulation, especially in the isolation measurement, and is shifted to 4.7 GHz. The resonant frequencies of the higher order modes are not predicted well the simulation. The shift in working frequency can be observed in the measurement as well, but only to a frequency of 5.62 GHz. The isolation of the measured beam splitter is with −45.7 dB better than the simulated isolation. As predicted by the simulation, the behaviour of cross and straight measurement around that frequency is very close to the theoretical expected one. The first higher order chip mode can also be seen in the measurement, but at a frequency of 7.4 GHz.

4.4. Simulations of interferometers

By cascading two 90° hybrid couplers of any design, an interferometer can be built. Since the simulations of beam splitters showed good results, similar to the theory, and lead to a better understanding of the measurements, it seems promising to perform simulations of interferometers as well. The simulations are performed on two different models. The first model is created by importing the structure from the file used to create the mask for

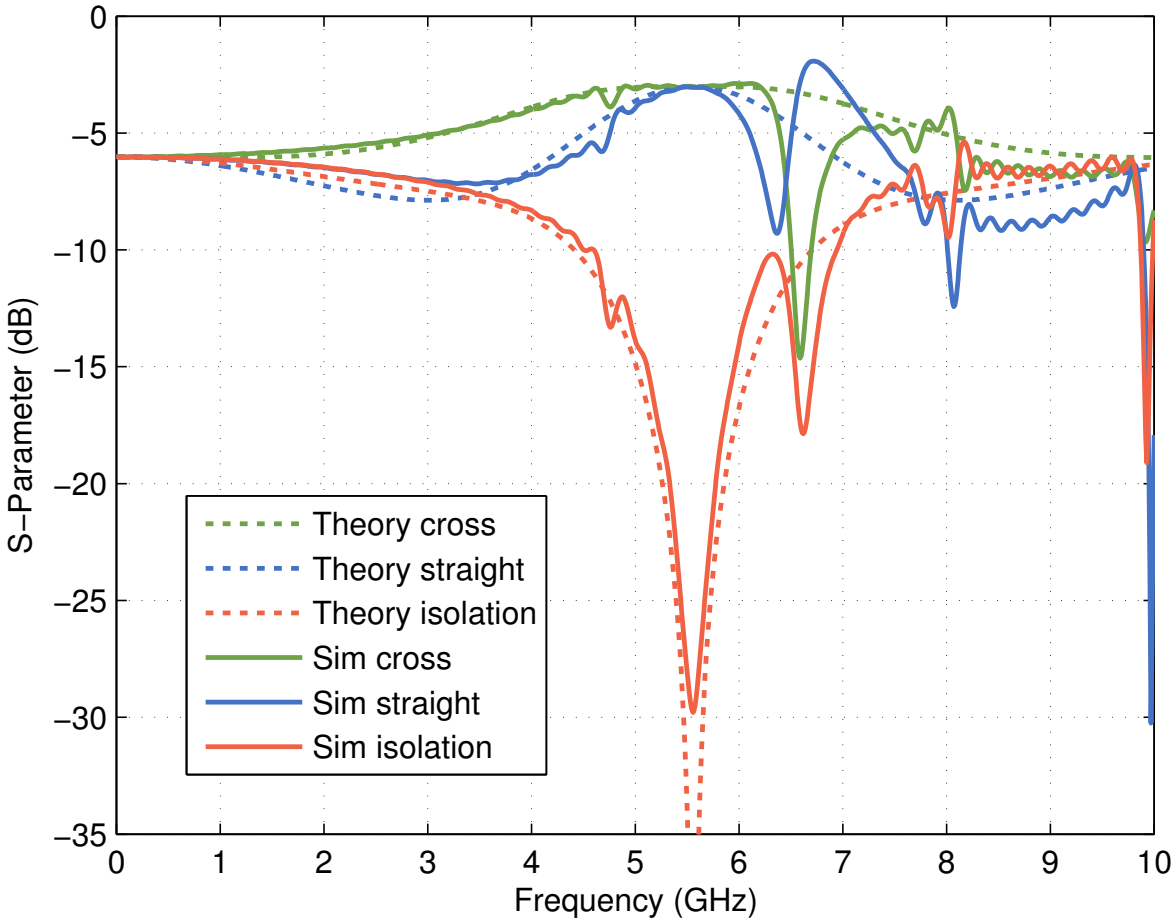

Figure 4.16: Results of the simulation of the beam splitter shown in Fig. 4.15 (continuous lines) in comparison to the theory of a beam splitter (dashed lines).

optical lithography. The second one is drawn in CST microwave studio. The latter lead to a drastic decrease in simulation time. This is achieved by a better performance of the simulation in curves. In the imported model, curves are approximated by polygons, in the second model, the curves are not approximated. Nonetheless, both models are shown in this part, as additional simulations are based on both models [see Sec. 4.5.1 ff.].

The first model is shown in Fig. 4.20. The additional structures on the chip compared to the design [compare Fig. 5.1] are markers used for electron beam lithography, that were not used in this thesis, but are included for future measurements with qubits coupled to the transmission line of the interferometer. The path between the two beam splitters is approximately 6 mm long. Similar to the beam splitter simulations, we observe multiple parasitic modes at 4.8 GHz, 7.5 GHz and at higher frequencies. As the

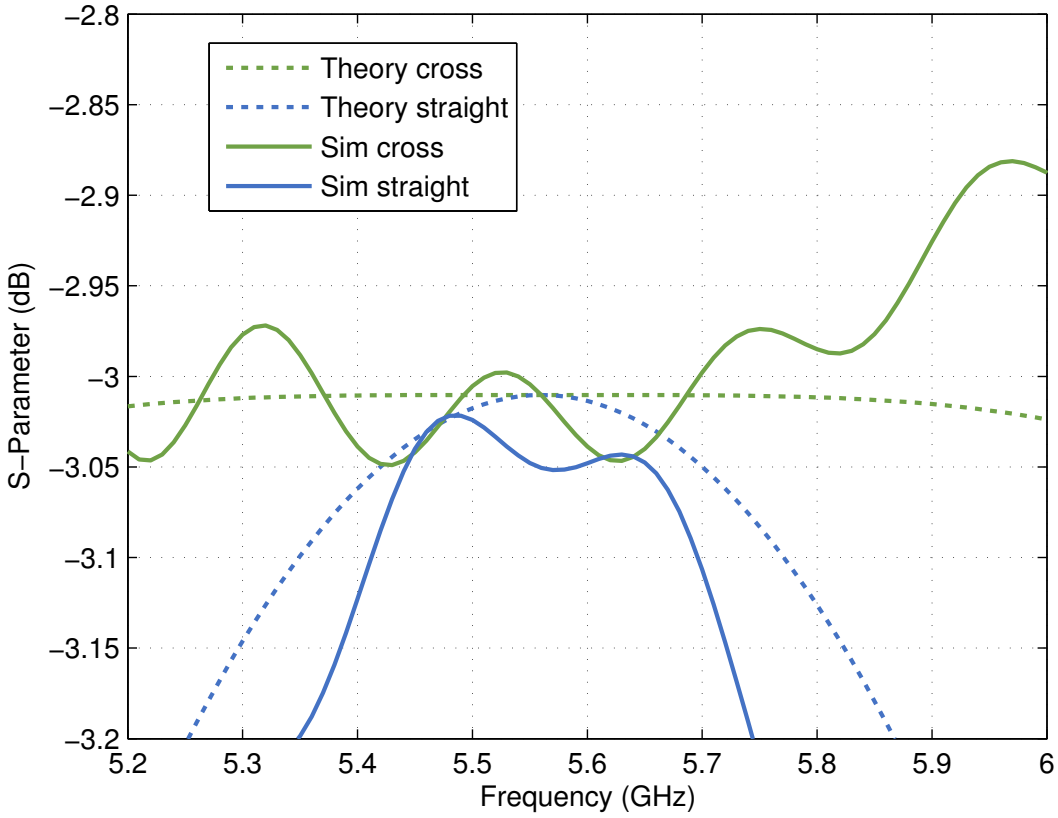

Figure 4.17: Zoom into the results of the simulation of the beam splitter shown in Fig. 4.15 (continuous lines) in comparison to the theory of a beam splitter (dashed lines) around the working frequency.

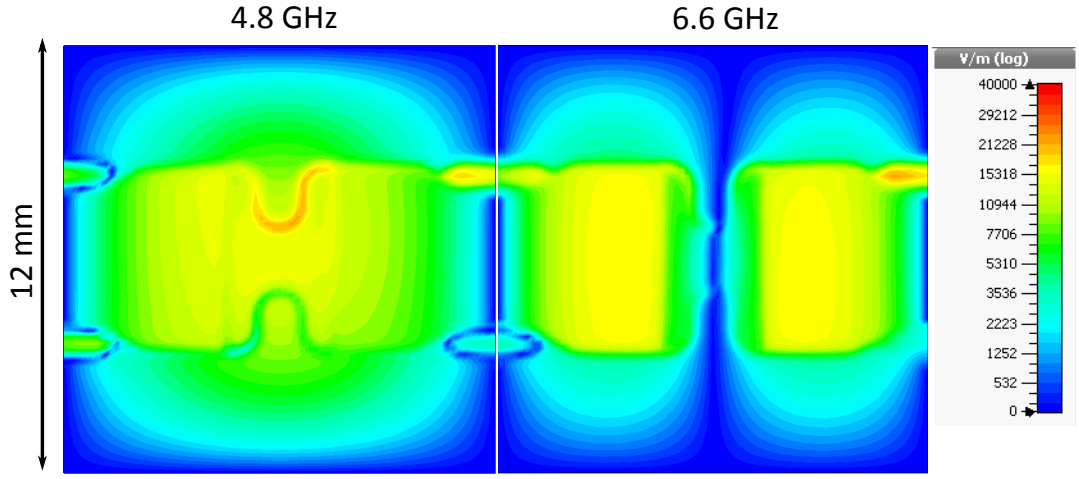

Figure 4.18: The simulated electric field on the backside of the meandered beam splitter. The left panel shows the first order of the observed chip mode at 4.8 GHz, the right panel shows the second order mode at at 6.6 GHz.

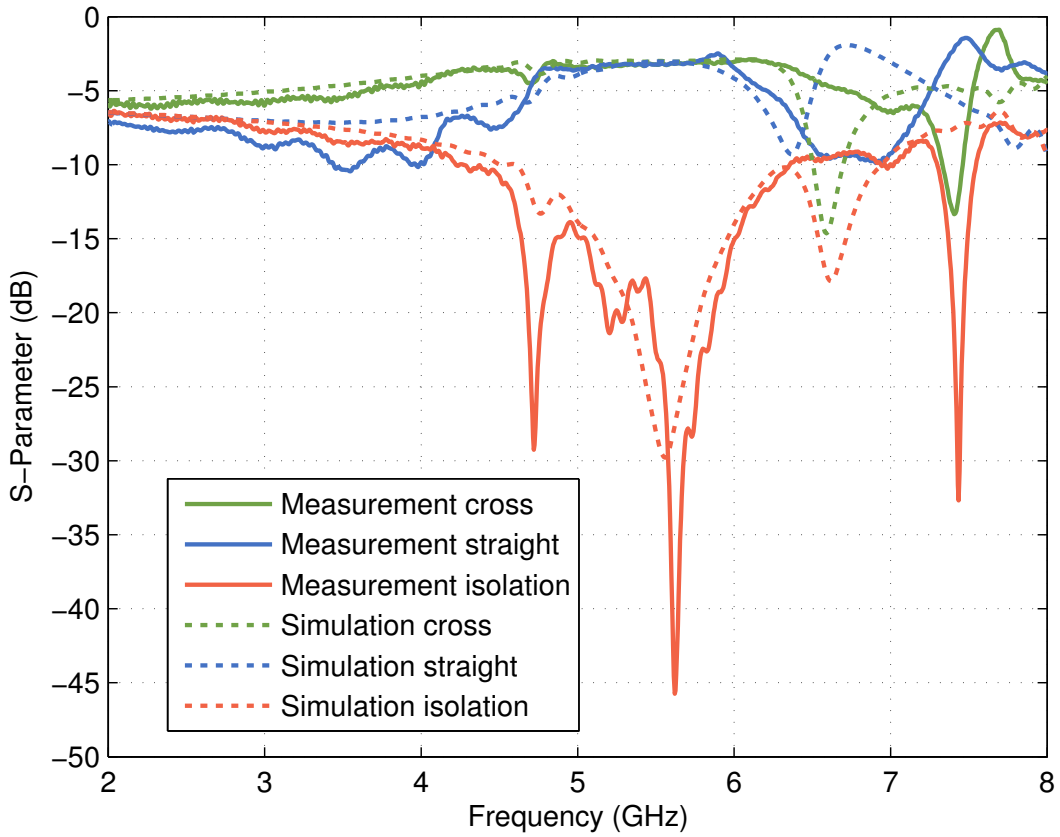

Figure 4.19: The simulation of the meandered beam splitter (dashed lines) in comparison to the measurement (continuous lines)[23].

length of the transmission lines between the beam splitters is longer than $\lambda_{\text{work}}/4$, the working frequency can be located in the second dip in the isolation [compare Sec. 2.4]. According to this, the simulation predicts a working frequency of 5.93 GHz. If we compare the S-parameters of the simulation to their theoretically predicted behaviour at this working frequency we do not observe a good accordance. By varying the working frequency of the theory calculations, we find a good agreement of simulation and theory for a frequency of 5.65 GHz [see Fig. 4.21], especially for the cross transmission of the simulation.

The latter is described well by its theory counterpart, although it deviates slightly for frequencies below 4 GHz and to a smaller degree around f_{work}, where the simulation predicts a smaller transmission of −0.3 dB in contrast to the perfect theoretical transmission. This can also be seen in the simulation of the isolation and the straight transmission. At the frequencies, where the theory predicts no transmission at the straight and isolation port, the minimal simulated transmission of the two is −21.6 dB and −40.0 dB, respec-

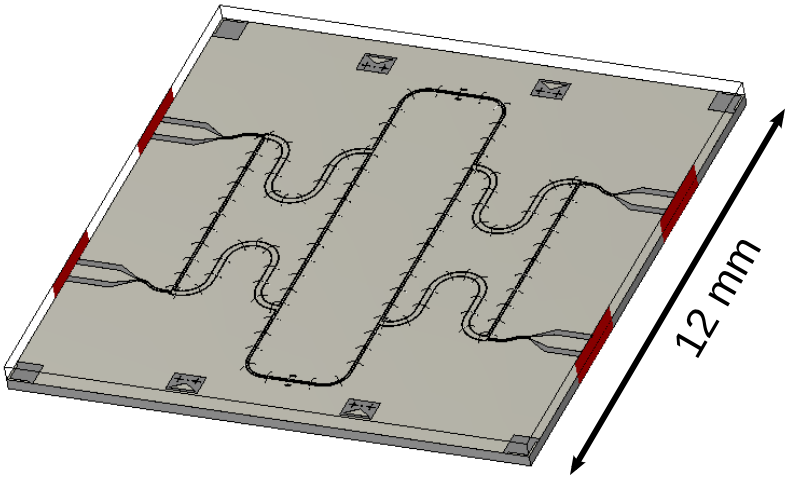

Figure 4.20: Model of interferometer with the structure imported from a GDSII-file.

tively. The two dip structure of the isolation also seems to be broadened, compared to the theory, which leads to a more difficult extraction of the working frequency as it can not be determined by simply identifying the frequency of the second dip. The behaviour around the working frequency might be caused by impedance mismatches or reflections, that are not included in the theoretical calculations. One of the possible reflection planes, are the t-junctions at the entrance and exits of the beam splitters.

As theoretical calculations show [see Sec. 2.4], the S-parameters of an interferometer depend strongly on the length L of the transmission line between the two beam splitters. Therefore, in the second model the length of this joint can be easily adjusted to account for different lengths of the joint. In the following part, two different simulations of the model, one with a short transmission line and the other with a longer one [see Fig. 4.22], are shown. The long transmission line is approximately 6 mm long, similar to the first interferometer simulation. The short one is approximately 3.8 mm long. For a working frequency of 5.75 GHz, $\lambda_{\text{work}}/4$ is approximately 5.2 mm. Therefore, the behaviour of the two interferometers should vary quite a bit.

Figure 4.23 exhibits the simulated results for the interferometer with long transmission line between the beam splitters. Similar to the previous simulation, the S-parameters vary from the simulation for frequencies below 4 GHz, but show similar tendencies. Again, the working frequency can not be easily extracted, but the behaviour of the simulated cross transmission resembles the theory for a working frequency of around

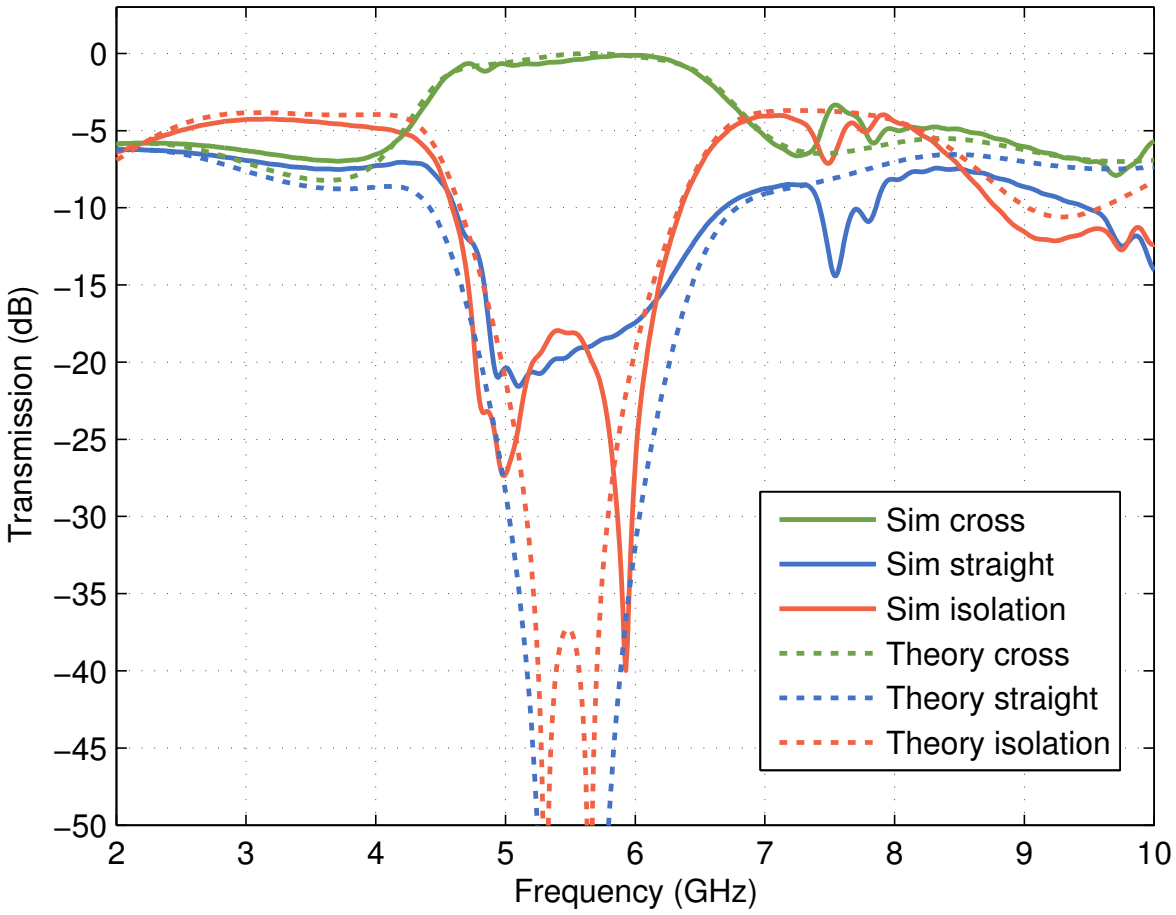

Figure 4.21: Comparison of the results of the simulation (continuous lines) with the theory curve (dashed lines).

5.56 GHz very well. This is also the simulated working frequency of the meandered beam splitter, that is cascaded to build the interferometer [see Sec. 4.3.2]. The cross transmission for the simulation and theory match very well, up to a frequency of approximately 6.5 GHz, except at 5.2 GHz, where we can observe the typical feature of the chip mode. The isolation and straight transmission exhibit a transmission between −17 dB and −25 dB and an oscillation, that is supposedly an artefact of the simulation, caused by the chip mode. The broadening of isolation and straight transmission around the working frequency, observed in the previous interferometer simulation, vanishes almost completely. The slope of the straight transmission is inverse to the one of the previous simulation at f_{work}. Note that this simulation was performed with a Rogers 3010 layer below the chip [see Sec. 4.5.1].

As expected, the simulation with shorter transmission lines between the beam split-

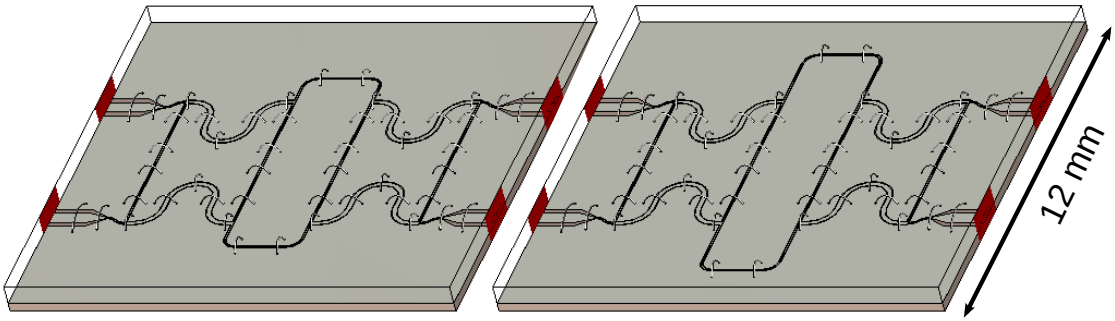

Figure 4.22: Model of interferometer drawn in CST with short joints (left panel) and long joints (right panel).

ters differs from the one with longer ones [see Fig. 4.24]. We observe again parasitic chip modes, similar to the ones in the previous interferometer simulations. The first three resonant frequencies are 4.5 GHz, 7.8 GHz and approximately 9.0 GHz. Comparing the simulation to the theory, we find a working frequency of 5.65 GHz. Around this frequency, the cross transmission is again very well matched to the theoretical calculation. The simulated isolation also follows the theory quite well, although the second expected dip in transmission can not be clearly defined since the simulation is superimposed with an oscillation for approximately 1 GHz starting at the working frequency. Nonetheless, the isolation is −47.8 dB. The dip in the straight transmission is broadened compared to the theory and is −23.8 dB deep at the working frequency. It is possible, that the broad structure in the simulation is caused by the first chip mode, as the transmission at the straight port drops significantly at the resonant frequency of the mode.

4.5. Improvements to previous simulations

The theory of the beam splitter and interferometer describes only a simplified model of the devices which does not consider, e.g., crosstalk between different transmission lines or the geometrical shape of the chip. Therefore, simulations show additional features which are not predicted by the theory. To account for these additional parameters, the following part focuses on different changes applied to the simulation models presented in Sec. 4.3 and 4.4. First, we have a look at the influence of a Rogers 3010 layer, to better match

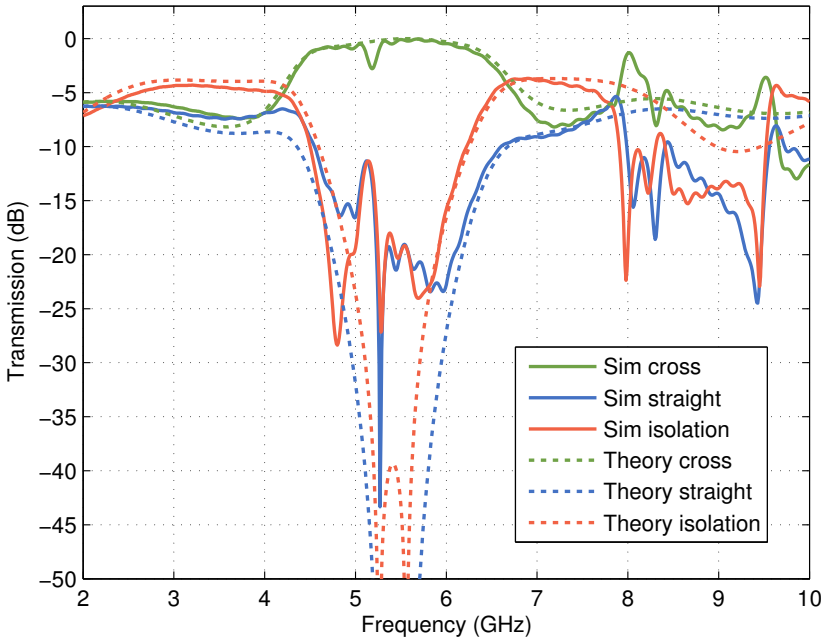

Figure 4.23: Comparison of the results of the simulation of an interferometer with long joints (continuous lines) with the theory curve (dashed lines).

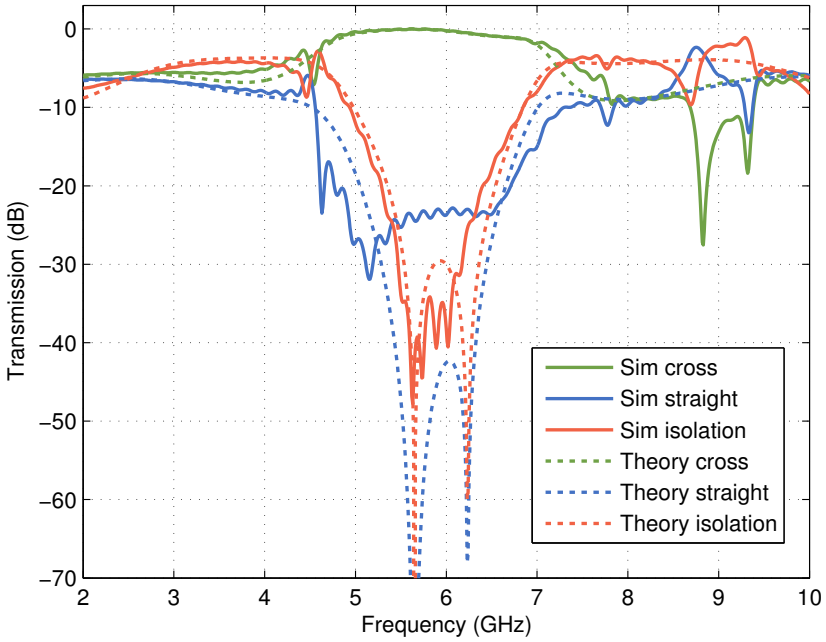

Figure 4.24: Comparison of the results of the simulation with short joints (continuous lines) with the theory curve (dashed lines).

the simulations and measurement. After that, we consider different ideas to improve the performance of the beam splitters and interferometers. The main focus is to suppress the different chip modes, that disturb the performance of the devices.

4.5.1. Simulations of a Rogers 3010 layer below an interferometer

To better understand the influences, that the surroundings have on the simulated devices, a simulation of an interferometer with short arms is performed with a 385 µm thick Rogers 3010 layer below the chip [see Fig. 4.25]. In the measurements, the chip is placed inside a pocket in a PCB, which consists of Rogers 3010. Therefore, the results of the simulation with this additional layer are expected to be closer to measurement results. If we take a look at the simulation results, we observe that the rough behaviour of the device did not change. Up to a frequency of 4 GHz, the simulation with dielectric layer and without it are almost the same. In contrast to this, introducing the Rogers 3010 layer shifted the frequency of the ground mode of the chip resonance from approximately 4.5 GHz to 5.2 GHz. This means, that the resonance is now closer to the working frequency and changes the behaviour around the latter. The working frequency itself did not change between the two simulations. Around the working frequency, the expected dip in the straight transmission is less broad in the simulation with Rogers 3010. The isolation did not change much in this frequency range, but is up to 10 dB worse in the immediate surrounding of f_{work}. The cross transmission of the two simulations differs slightly starting at a frequency of 6 GHz. The simulation without Rogers predicts a higher transmission at this port. The reason for this might be the introduction of a new loss channel with the implementation of the Rogers 3010. The second chip mode is shifted to a higher frequency of approximately 8 GHz from 7.6 GHz and is increased in intensity. This shift can also be observed in higher order modes. If we compare these results to the measurements of an interferometer [see Chapter 5], we observe that despite the fact that the measurements are performed with Rogers 3010 below the actual chip, the frequency of the first chip mode, is similar to the one of the simulation without Rogers. This can be explained by the size of the Rogers layers. In the simulation, the additional dielectric is of the same size as the chip, i.e., 12 mm × 12 mm, but in the measurement the Rogers is part of the whole PCB, which is 4 cm × 4 cm large. This leads to different boundary conditions, which may not allow the chip mode to form inside the Rogers. Therefore, the larger Rogers 3010 layer might not affect the frequency of this mode.

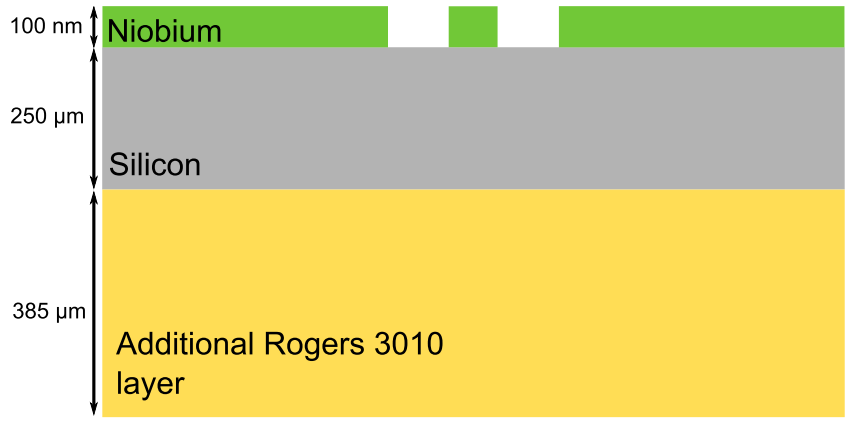

Figure 4.25: Sketch of the structure of the model with an additional Rogers 3010 layer.

4.5.2. Interferometer with on-chip vias

Simulations of PCBs have shown, that vias in general and their placement in particular can improve the performance of microwave devices. To suppress parasitic modes, we present a model of an interferometer, with vias implemented around the transmission lines on the chip [see Fig. 4.27]. It is important to note, that the boundary conditions in the simulation set a metal box around the model. This means, the vias connect the ground plane of the chip to said metal plate under the chip. Therefore, they form a connection of the different parts of the ground plane. To improve the results, this first model has a high via density. We observe a behaviour of the S-parameters of the interferometer that resembles the results of the simulation without the on-chip vias. At all frequencies, short of the resonant frequencies of the chip mode, the S-parameter stay approximately the same [see Fig. 4.28]. The resonant structures of the chip mode vanish completely. At 4.8 GHz, where we can observe the first chip mode in simulations without on-chip vias [see Fig. 4.29 (left panel)], we can see the structure of the CPW mode, which is expected if no parasitic resonances are present [Fig. 4.29 (right panel)]. The same holds true for higher order modes, e.g., the second order mode at 7.6 GHz. In conclusion, the on-chip vias suppress the parasitic modes. In an experiment, this setup is rather hard to implement, since the building of vias in a silicon substrate, especially in such high numbers, is very demanding and so far unexplored in the Walther-Meissner-Insitut. Therefore, it is necessary to investigate further ideas, that may be easier to achieve in experiments.

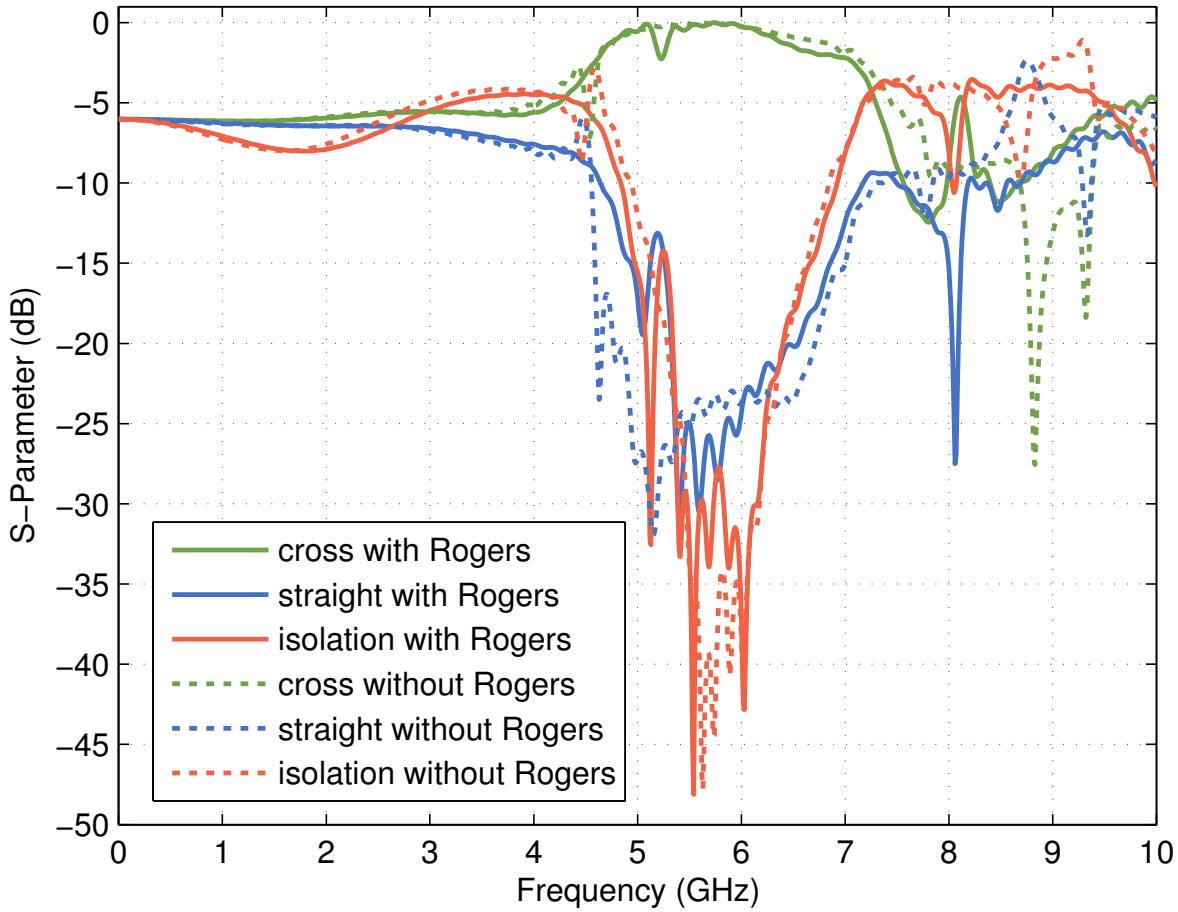

Figure 4.26: Results of the simulation with a Rogers 3010 layer in comparison to a simulation without the layer.

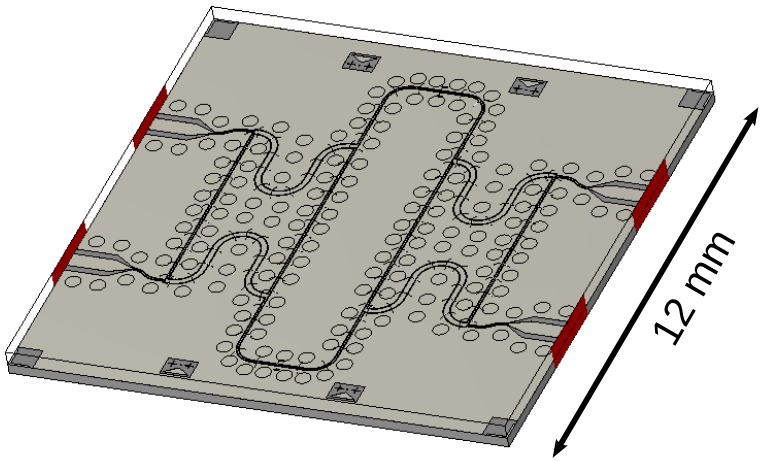

Figure 4.27: Picture of the model of an interferometer with on-chip vias.

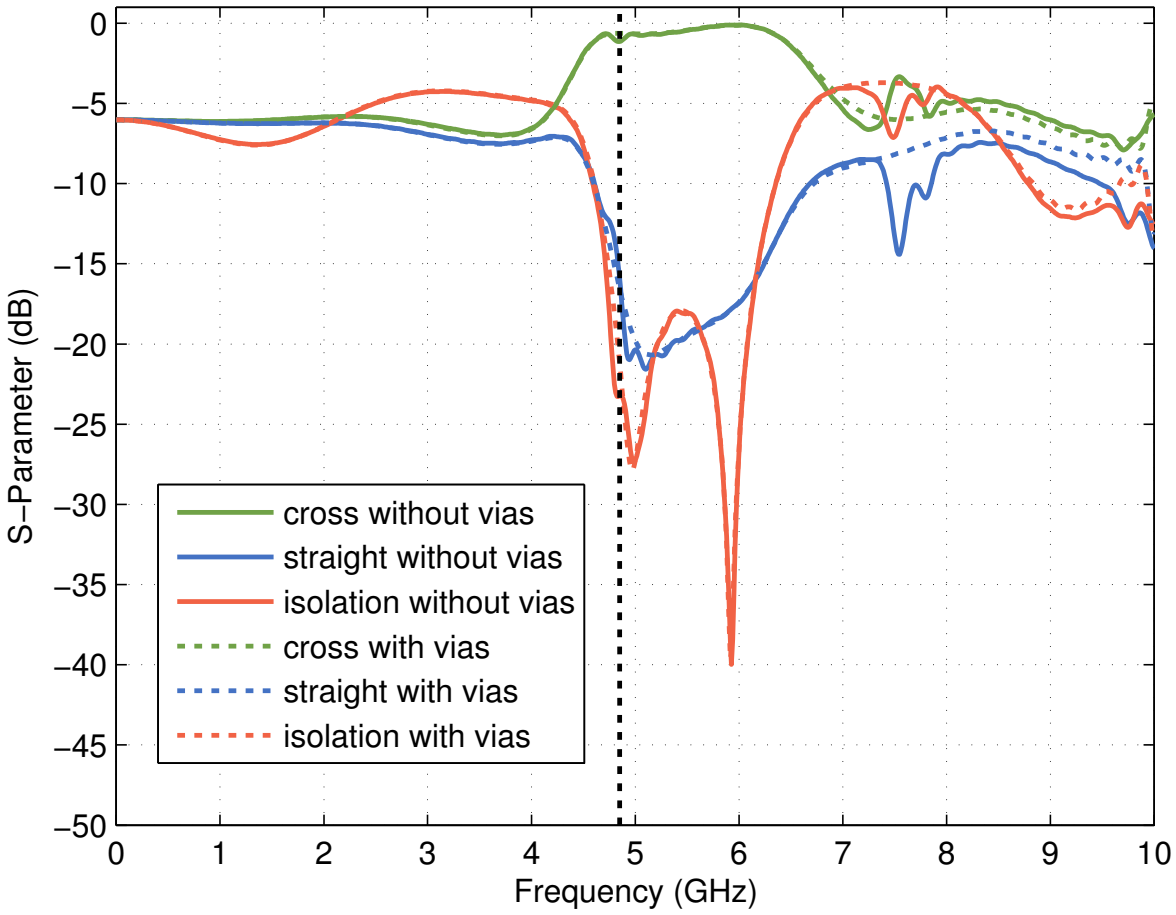

Figure 4.28: Simulation results of an interferometer with on-chip vias in comparison to the simulation of the same model without on-chip vias.

4.5.3. Simulation of a beam splitter with parts of the substrate removed

An easier option than on-chip vias, would be to cut off parts of the substrate and of the ground plane. By changing the shape and size of the chip in this way, we hope to shift the resonances of the chip mode to frequencies far away from the working frequency, or to remove their appearance altogether. To validate the effects of this method, we simulate a beam splitter with parts of the substrate between the ports on both sides removed [see Fig. 4.30].

If we compare the simulation of the straight beam splitter from Sec. 4.3, which is the basis for the new model, with the simulation including holes in the substrate, we observe, that, as expected, the resonance frequency of the chip modes are shifted. Unexpectedly, the

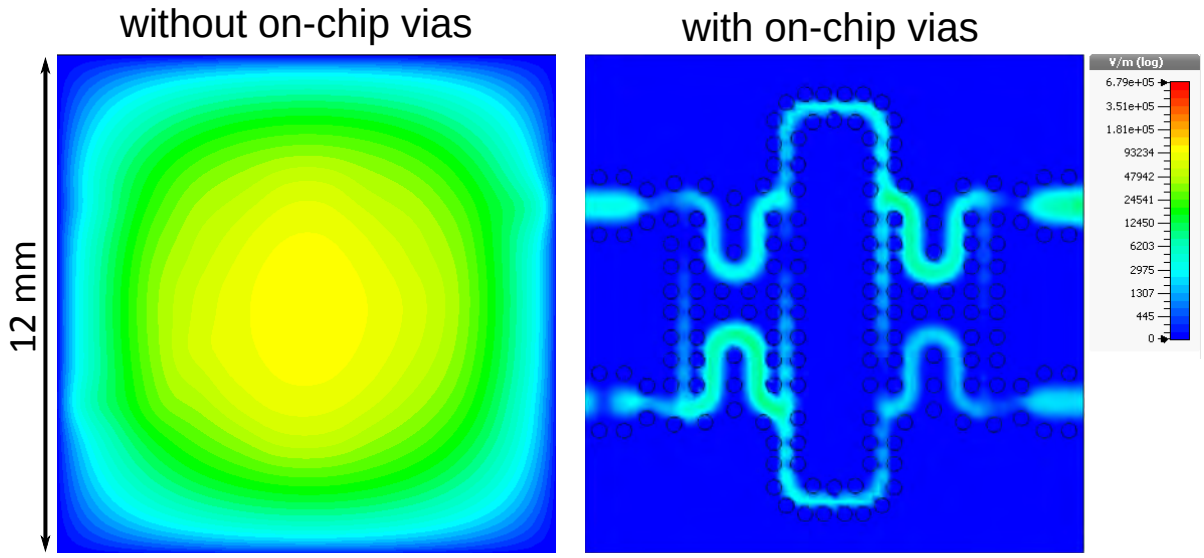

Figure 4.29: Picture of the electric field on the backside of an interferometer with on-chip vias (right panel) and of an interferometer without them (left panel) at 4.8 GHz.

resonance frequencies are lower than with the full substrate. For example, the first mode observed in this simulation is shifted down by approximately 0.6 GHz to a frequency of 7.0 GHz. In addition, the working frequency of the beam splitter is shifted from 5.83 GHz to 5.60 GHz. The cross and straight transmission improved their behaviour in respect to the theoretical calculation. The crossing of the two parameters around the working frequency vanished and we observe a transmission of −3.1 dB and −3.0 dB at the straight and cross port, respectively. Other than that, there seem to be no major differences between the two simulations. All in all, we are able to change the frequency of parasitic modes by cutting away parts of the chip, but are unable to shift them to frequencies far away from the working frequency or to suppress them completely.

As vias already proved to enhance the behaviour of microwave devices, especially by suppressing the parasitic modes, the arc, created by removing of part of the substrate, is now coated with perfectly conducting material [see Fig. 4.30 (zoom)]. The results of this simulation are compared to the theory of a beam splitter in Fig. 4.32. We observe, that the parasitic resonant structures vanished from the simulation, and the simulation matches the theory really well. The working frequency is 5.63 GHz and the isolation at this frequency is −34.6 dB. The splitting of the cross and straight transmission is only 0.04 dB.

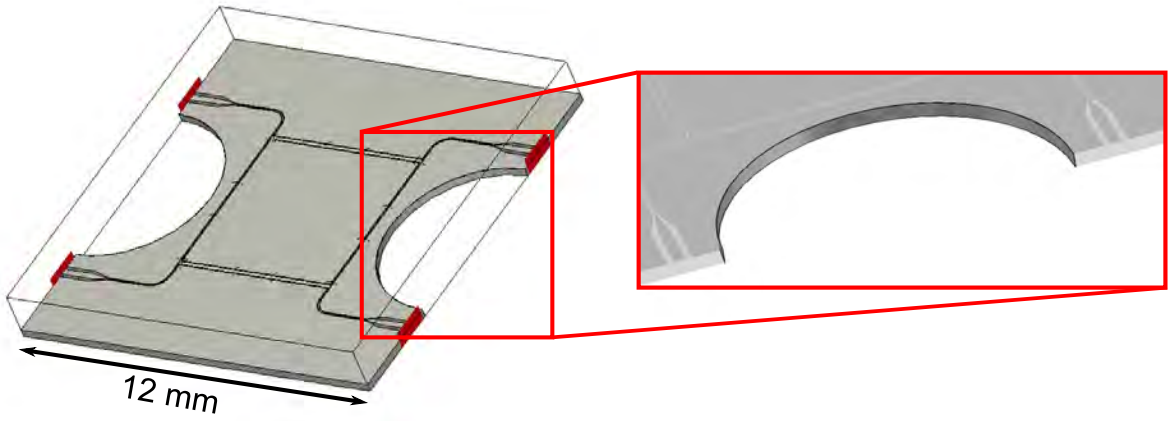

Figure 4.30: Pictures of a beam splitter model with holes in the silicon wafer. The highlighted shape in the zoomed picture is either coated with metal or left empty in different simulations.

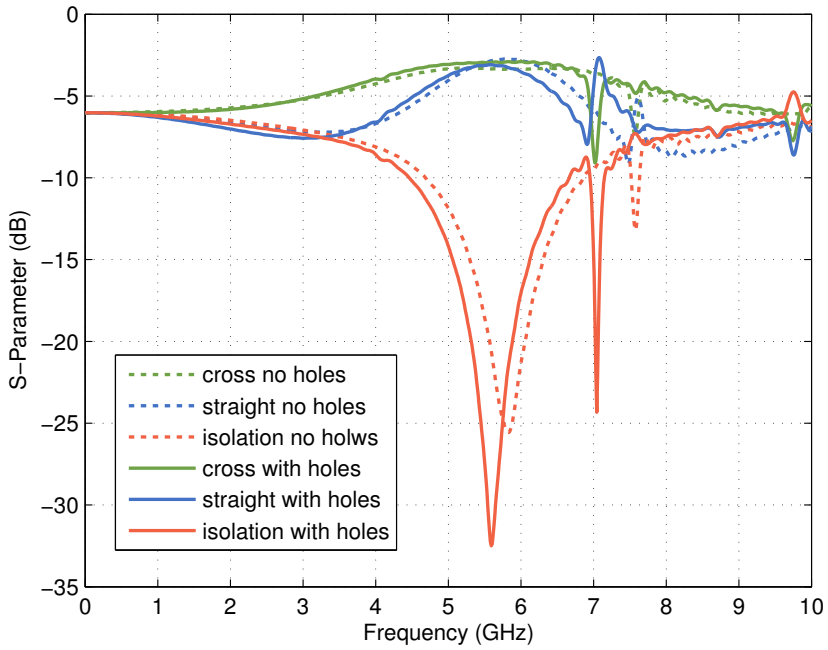

Figure 4.31: Simulation results of the model with holes, but without metallized arc.

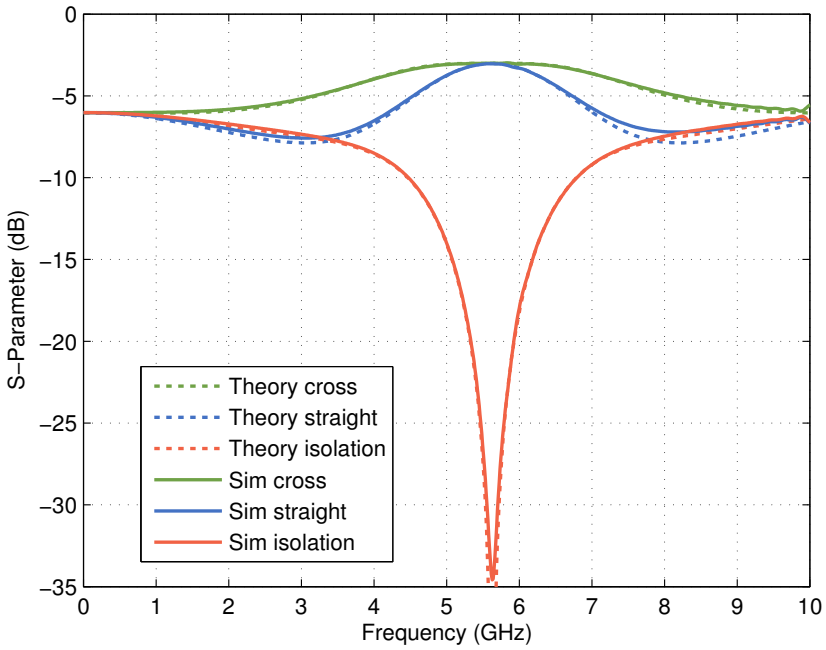

Figure 4.32: Simulation results of the model with holes and with metallized arc, in comparison to the theory.

4.5.4. Interferometer consisting of beam splitter with holes

The simulation of the straight beam splitter with parts of the ground removed and coated with a metal layer has proved that with some small adjustments, the behaviour of the device can be largely improved. To see whether this holds true for interferometers, we perform a simulation of an interferometer built with the improved straight beam splitter [see Sec. 4.5.3]. Two of the latter are cascaded after one another, leading to a 12 mm × 24 mm chip, with holes on either port side and in the middle. The joint between the two beam splitters is with 8.2 mm larger than in the previously simulated interferometer, leading to a different theoretical expectation for the behaviour of the S-parameters. Looking at the results of the simulation in comparison to the theory curves [see Fig. 4.34], we observe a very good matching of simulation and theory with a working frequency of 5.56 GHz. The structures around the working frequency of the simulation are broadened in comparison to the theory, similar to previous interferometer simulations [see Sec. 4.4]. We observe two dips in isolation and straight transmission, one at 4.4 GHz and the second at 5.7 GHz, opposed to the theoretical prediction, with one dip at 4.5 GHz and one at the working frequency. A third dip in these two transmissions can be seen at 8.3 GHz in both simulation and theory. The simulated transmission through

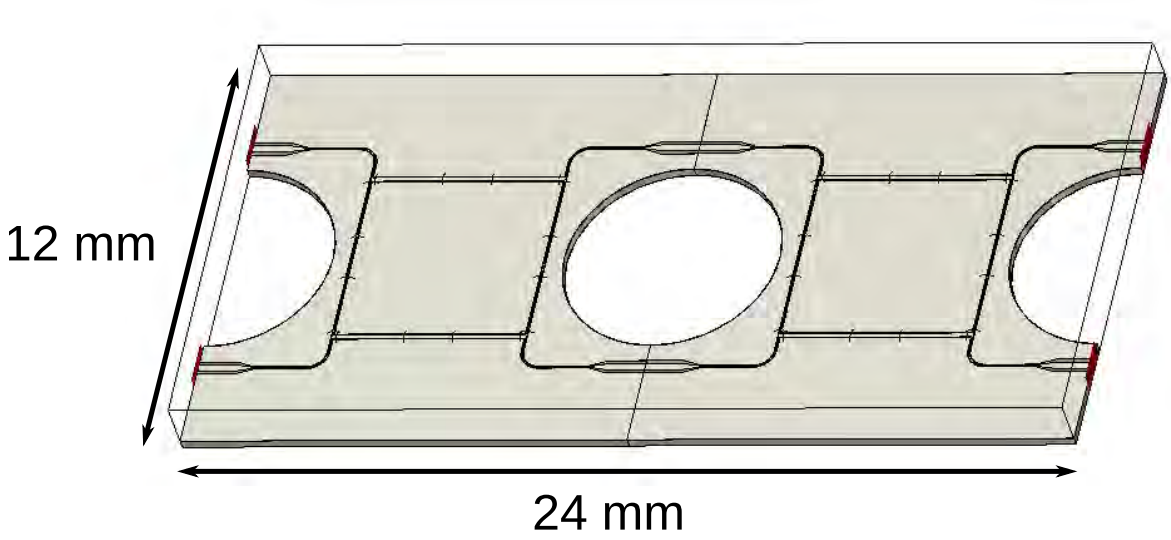

Figure 4.33: Model of Interferometer consisting of two beam splitters with holes.

the cross port at the working frequency is with $-0.04\,\mathrm{dB}$ almost perfect. Isolation and straight transmission are $-60.0\,\mathrm{dB}$ and $-46.8\,\mathrm{dB}$ near f_{work}.

With this simulation we can prove, that it is possible to build a very well working interferometer model using small variations. Since the measurement setup is optimized for smaller chips, this interferometer model is not usable at the present.

4.5.5. Interferometer with smaller holes

For combining the interferometer with other components such as single photon sources, the size of the interferometer has to be optimized. Therefore, the improvements shown in Sec. 4.5.3 ff. have to be implemented onto an interferometer model with meandered beam splitters to account for the available space in the measurement setup. In addition to this, the large holes in the substrate might cause the chip to become flawed, and therefore cause cracks or even break the chip. Therefore, a model with smaller holes has been simulated [see Fig. 4.35]. The results of this simulation show, that the parasitic modes, seen in the simulation without the vias, vanish [Fig. 4.36]. The S-parameters are overall smoother, especially the isolation and straight transmission around the working frequency. The transmission of the latter two is slightly increased. It is very important, that the vias are connected to a ground plane of some sort. A similar simulation, including a Rogers 3010 layer below the silicon chip, show no improvements to the

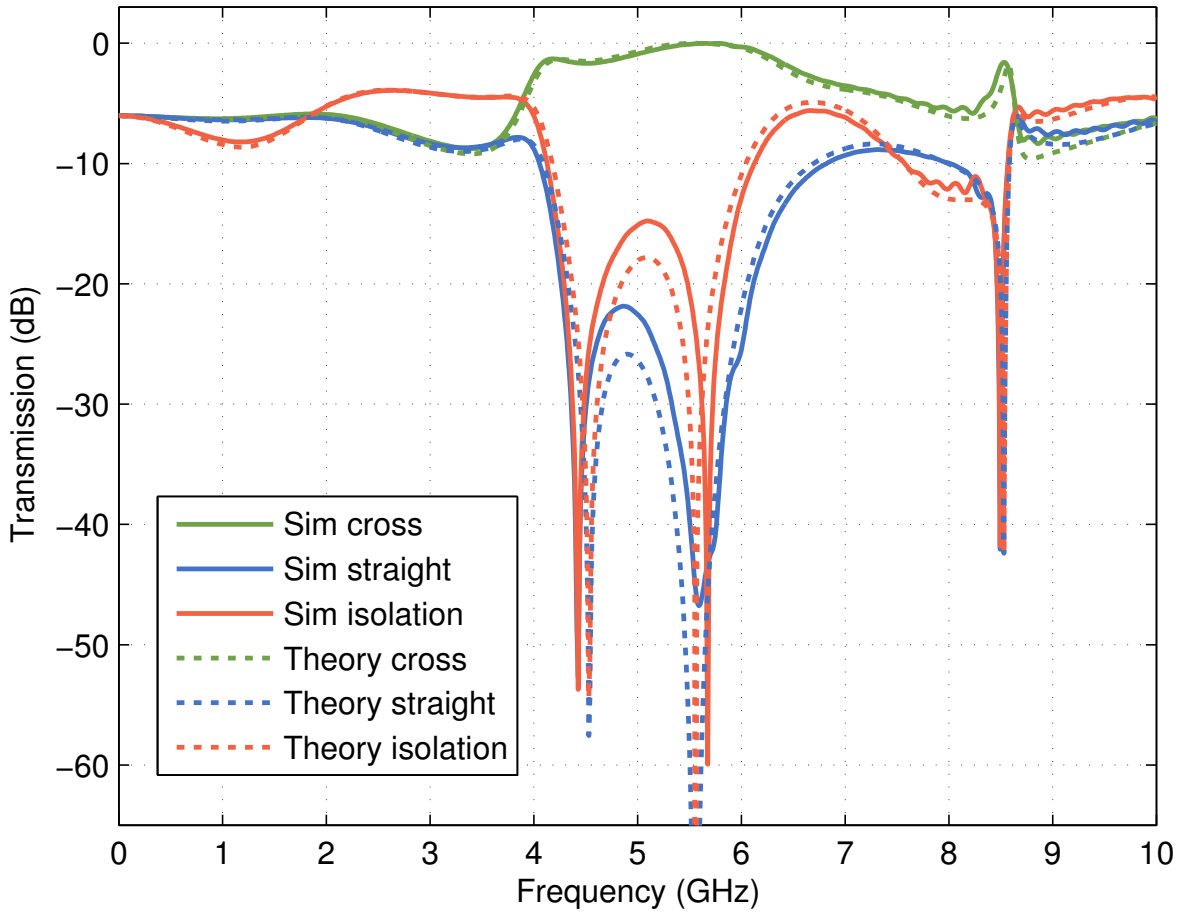

Figure 4.34: Results of the simulation of an interferometer consisting of two beam splitters with holes [Fig. 4.33] compared to theory.

simulation without vias. Although, extending the vias through the additional dielectric does lead to a similarly improved behaviour.

The simulation shows, that it seems to be possible to suppress the parasitic chip mode by implementing three metal plated vias on the chip. In order to use the improvements in measurements, it is important to investigate the possibilities of on-chip via construction at the Walther-Meissner-Institut.

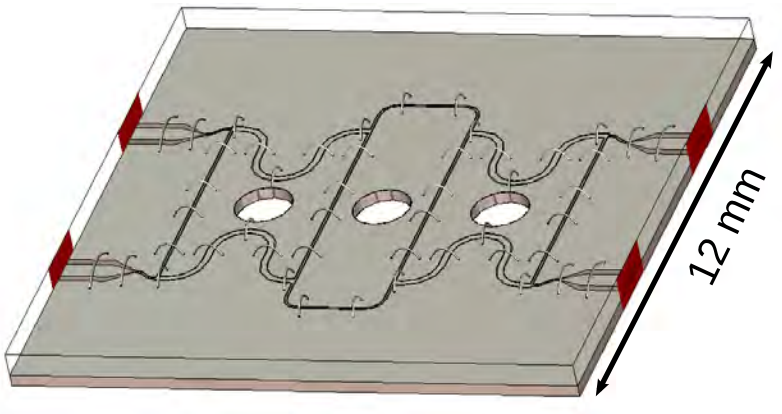

Figure 4.35: Model of Interferometer with three vias and with a Rogers 3010 layer.

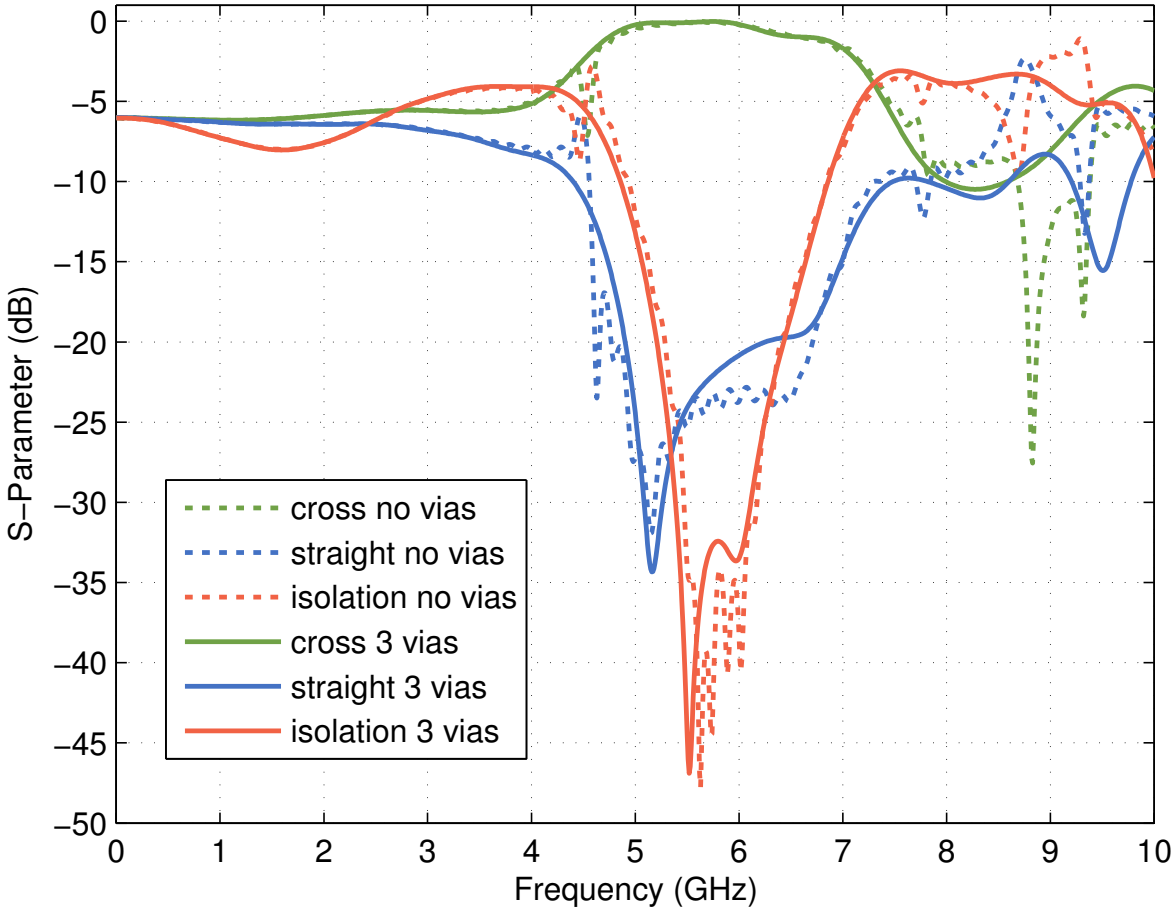

Figure 4.36: Results of the simulation of an interferometer with three vias.

5. Experimental results

In the following section multiple measurements of interferometers are presented. The measured devices are interferometers consisting of two cascaded beam splitters with meandered arms. One of the latter has a long joint between the two beam splitters, while the second and third interferometer are equipped with short transitions. An antenna and additional gaps to include a transmon in later measurements are added to the third one.

5.1. Measurement of an interferometer with long joints

In the first measurement the two meandered beam splitters are connected by a joint with a length of 6 mm [see Fig. 5.1 (left panel)]. The picture of the sample shows the arrangement of bonds on the chip and between PCB and chip [Fig. 5.1 (right panel)]. The calibration for this measurement was performed without 50 Ω terminations on the unused ports [see Sec. 3.2.5], which leads to artefacts, i.e., peaks, in the measurement. We observe these artefacts, for example, at 2.9 GHz, 3.9 GHz and 4.4 GHz [see Fig. 5.2]. Other than that, the measured S-parameters show expected behaviour. Starting at a frequency of approximately 5.4 GHz up to a frequency of 6.3 GHz, we observe transmission with almost full power at the cross port, which is the main goal of the interferometer. The isolation is damped by up to −43.2 dB and the straight transmission by approximately −27.5 dB in this frequency range. Parasitic resonances, that are not predicted by the theory, can be seen at 4.7 GHz, 7.1 GHz and 9.2 GHz.

Judging by the best damping of isolation and straight transmission, we can define the working frequency as 5.97 GHz. By comparing the measurement to the theoretical calculations with a working frequency of 6.0 GHz, which fits the data the best, we observe that a second dip in isolation just below the working frequency, predicted by the theory, can not be seen in the measurement. In addition to that, the straight transmission is almost

flat around the working frequency as opposed to a two dip structure, as can be seen in the theory. This might stem from different electrical lengths of the two joints between the beam splitters [see also Sec. 2.4 and 5.3], caused by impurities on one side of the chip, or maybe by variations in bond placement or slightly altered impedances in the beam splitter arms. The theory also predicts a broader range of good cross transmission. Above a frequency of approximately 7 GHz, measurement and theory curves only match very roughly, as the measurement shows multiple resonant features.

The latter can be explained if we compare the measurement with a simulation of the interferometer. For this comparison we use the first simulation discussed in Sec. 4.4 [see Fig. 4.21], as it is the simulation with the model closest to the measurement. The resonance at 4.8 GHz is very well described by the simulation. As discussed in the simulation part of this work, these resonances are field modes inside the silicon chip. This particular one is the ground mode. The resonant frequency of the higher order modes are predicted by the simulation to be at higher frequencies as in the measurement. Nonetheless, we can assign the resonant structures at 7.1 GHz and 9.2 GHz in the measurement to similar structures in the simulation and thus explain their origin. The simulation shows that the two resonances in question stem from modes in the silicon chip as well.

The deviation of measurement from the theory below 4 GHz is described well by the simulation, implicating that this is due to the geometry of the interferometer and not due to external influences. Between approximately 4 to 5 GHz, the cross transmission of measurement and simulation vary from each other due to small oscillations in the measurement, which might stem from reflection planes in the measurement setup, e.g., at the transition between different cables. From there to a frequency of 7 GHz, the cross transmission is very well explained by the simulation, not taking into account the calibration artefacts. Similar to the theory, the simulation predicts a first dip in isolation well below the working frequency, that is not observed in the measurement. The second dip in the simulated isolation on the other hand, is similar to the dip in the measured isolation. Although the measurement shows a broader dip, the simulated and measured one are only 50 MHz apart. This indicates a possible different theoretical working frequency of the measured interferometer. The simulation is similar to the theoretical behaviour of an interferometer with 5.56 GHz, but features a broader behaviour, especially in isolation. Since the first dip in isolation is not observed in the measurement, this broader behaviour leads to the assumption of a higher working frequency. For practical uses,

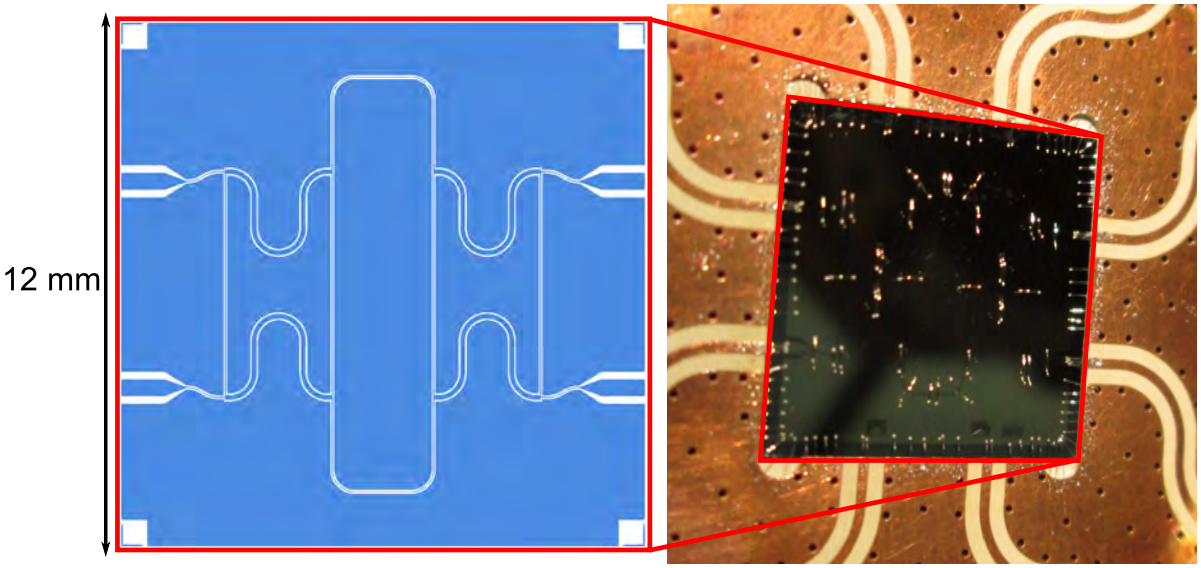

Figure 5.1: Design of the interferometer used for the first measurement, with a photograph of the sample inside the PCB, connected with bonds.

the theoretical working frequency is not as important as the actual observed working frequency, defined by a good isolation and low transmission at the straight port, in addition to high transmission at the cross port, which defines a sweet spot for future applications. Nonetheless, when designing an interferometer, it is necessary to predict the working frequency of the device, which in this case, can be done by simulation. The straight transmission of the simulation and measurement do not match well, as the simulation predicts a higher transmission of more than $-20\,\mathrm{dB}$, while the measurement is damped by more than $-30\,\mathrm{dB}$ at its lowest point.

Overall, the measurement shows very good behaviour, especially around 6 GHz, which is promising for additional future experiments. Other than for the missing first dip in isolation, it is well described by theory and simulation.

5.2. Measurement of an interferometer with short joints

In future measurements, qubits will be placed in gaps in the transmission lines between the beam splitters [see Fig. 5.5 (middle and right panel)]. To control these qubits, antennas are needed near the qubit site. In a step towards these designs we measure an interferometer with shorter joints [Fig 5.5 (left panel)], in order to make room for antennas. The design frequency for this device is 5.4 GHz. This frequency was chosen

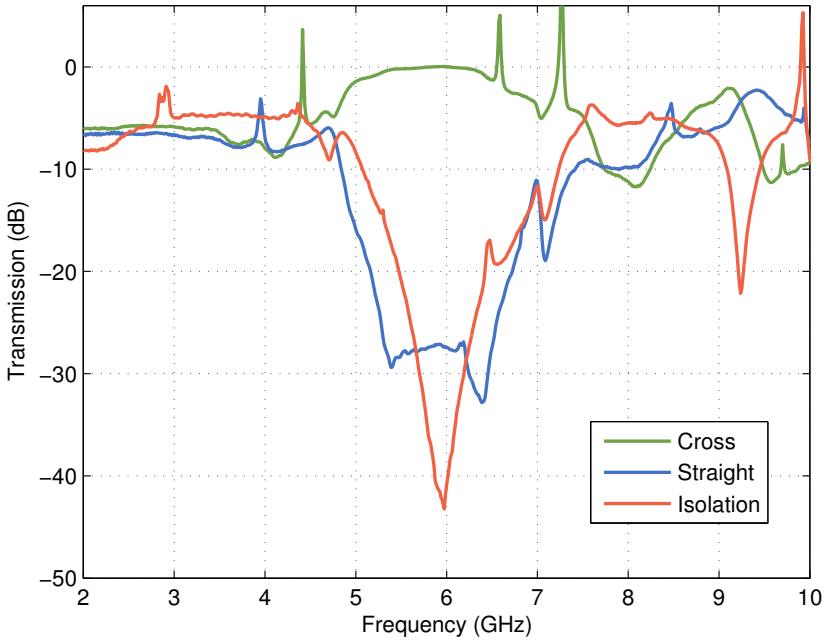

Figure 5.2: Measurement of the interferometer with long joints depicted in Fig. 5.1. Due to unterminated PCB lines in the calibration, the measurement shows multiple peaks, that are no features of the measured device.

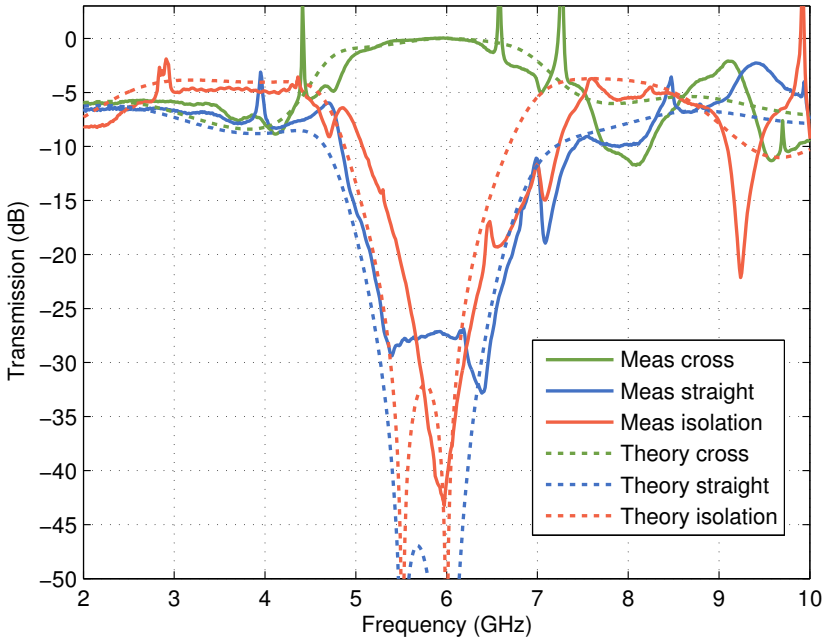

Figure 5.3: Measurement of the interferometer with long joints depicted in Fig. 5.1 in comparison to the theory of the interferometer.

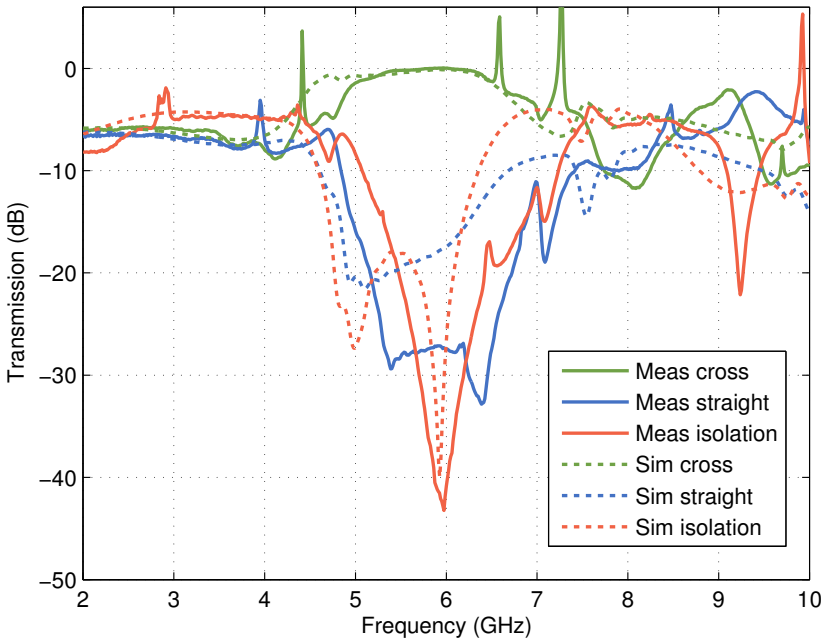

Figure 5.4: Measurement of the interferometer with long joints depicted in Fig. 5.1 in comparison to the simulation of the interferometer.

since the Josephson parametric amplifier built by Edwin Menzel [24], that may be used in combination to the interferometer in future experiments, performs well around this frequency. Unfortunately, the calibration used for this measurement is outdated, since the measurement is performed some months after the calibration has been made. Thus, we are only able to perform a rough analysis, since the exact transmission at the working frequency, for example, is not reliable. Similar to the first measurement, we observe parasitic resonances, that are not further discussed in this section [see Sec. 4.4 and 5.1].

Compared to the theoretical calculations with a working frequency of 5.4 GHz, the cross transmission is with −2.0 dB at the working frequency rather low, possibly due to the calibration. The isolation and straight transmission show multiple dips between 5 GHz and 7 GHz as predicted by the theory, in contrast to the measurement of the interferometer with long joints. In this frequency range, the behaviour of the two is broadened, leading to dips in transmission lower and higher than the theoretical prediction, respectively. The straight transmission is at its lowest point of −41.7 dB at 5.3 GHz and the isolation is damped by up to −26.8 dB at 5.1 GHz. At the working frequency, the transmission at the isolation and straight port are −19.1 dB and −26.9 dB. The simulation of the device predicts a similar behaviour around the working frequency, al-

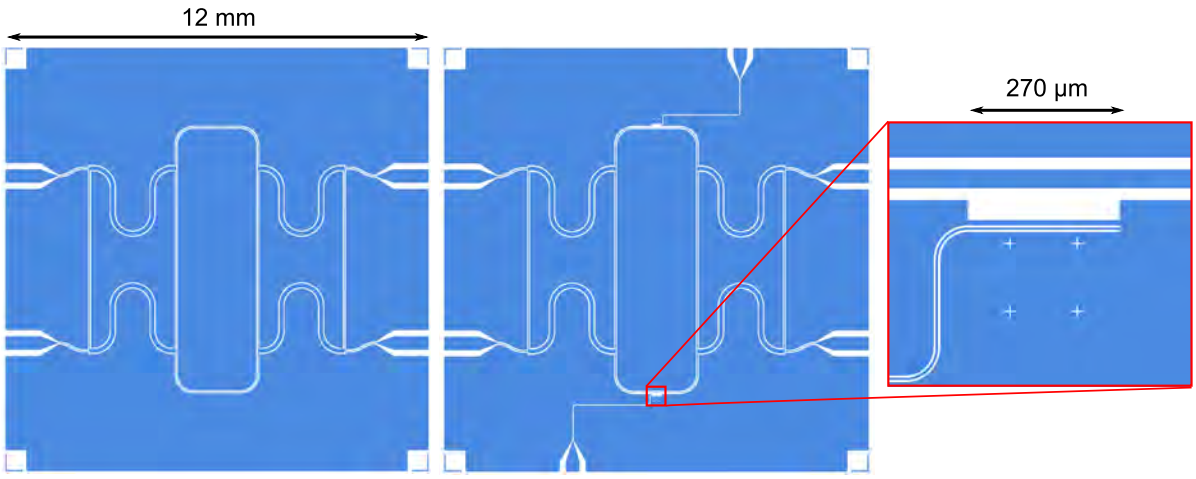

Figure 5.5: Picture of the design for transmon placement and antennas in the arms of the interferometer. On the left the design with shorter joints connecting the two beam splitters is depicted. In the middle is a picture of the design with space for two transmon qubits and two antennas to control them. To the right is a zoom of the transmon site.

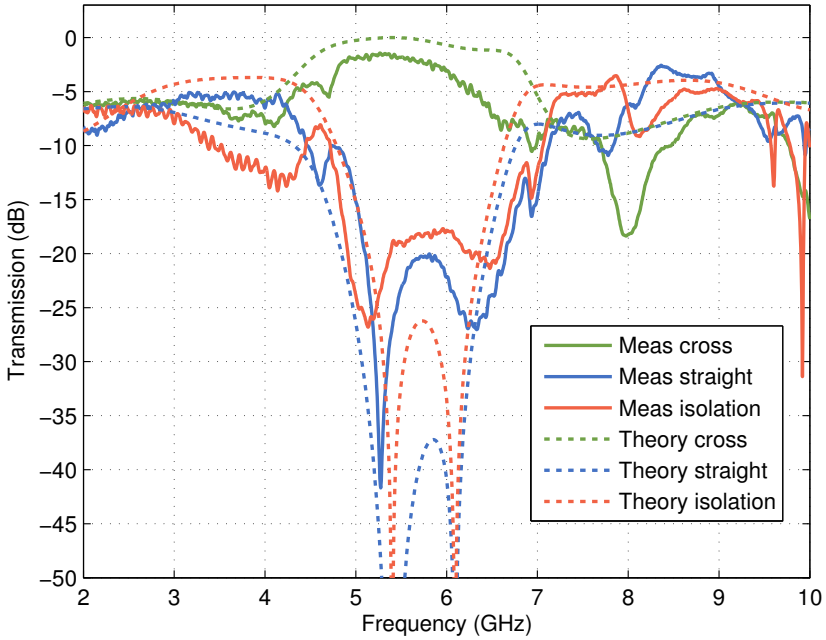

Figure 5.6: Measurement of the interferometer with shorter joints in comparison to the theory.

though it shows deeper isolation and a different shape of the straight transmission [see Fig. 5.7].

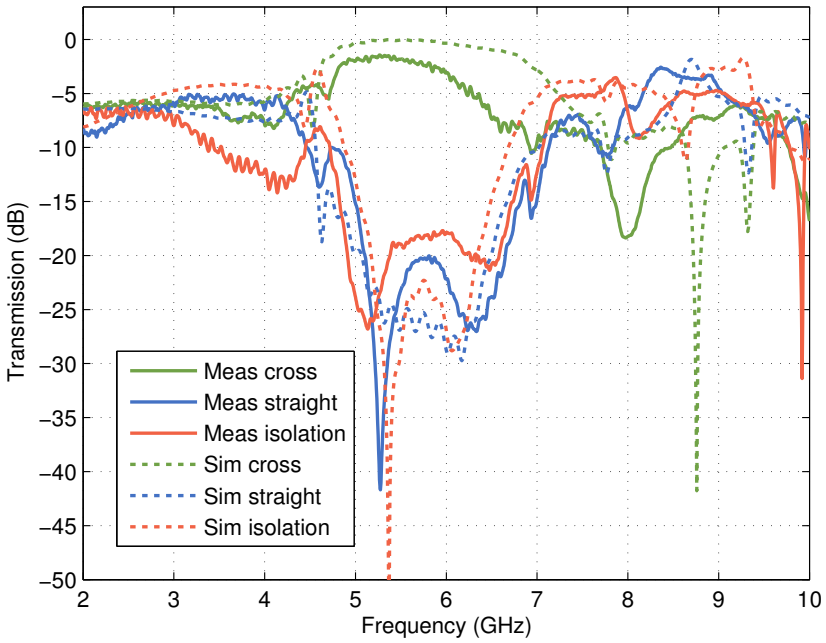

Figure 5.7: Measurement of the interferometer with shorter joints in comparison to the simulation data.

5.3. Measurement of an interferometer with an antenna

In order to estimate the effect of antennas near the transmission line between the two beam splitters, that form the interferometer, we measure a device equipped with one antenna at the joint [see Fig. 5.8]. By adding only one antenna, this measurement also gives information about the behaviour of the interferometer for an asymmetrical setup. The interferometer also contains two additional gaps for transmon qubits in future experiments. Figure 5.9 shows the measurement in comparison to the theoretical calculations for this system. These calculations include asymmetrical conjunction pieces between the two beam splitters, meaning different length of the two pieces. The best fit between theory and measurement could be achieved for a difference of 400 µm in the length of the latter and a working frequency of 5.75 GHz. This leads to a very good description of all three measured transmissions. Altered impedances in one or both of the conjunction arms, caused by the transmon sites and the antennas, could also contribute to the measured behaviour. Similar to the other measurements, we observe parasitic resonances, that are not further discussed in this section [see Sec. 5.1 and 4.4].

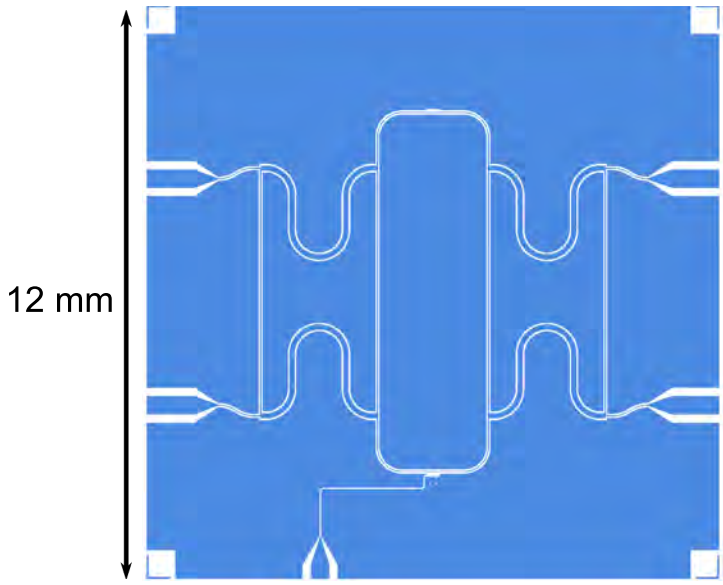

Figure 5.8: Design model of the interferometer with two transmon sites and one antenna.

The trend of the measured cross transmission is similar to the theory, although the measurement shows a slightly lower transmission. At 5.75 GHz the latter is −0.46 dB as opposed to a transmission with full power. This might be due to the introduction of transmon sites, which change the impedance in the joints between the beam splitters. Around the working frequency the isolation shows two dips with a depth of approximately −34 dB, in good accordance to the theory. We observe two dips in the straight transmission at 5.4 GHz and 6.6 Ghz, with a depth of approximately −28 dB. The one at 6.6 GHz matches very well with the theory, while the first dip is deeper than expected.

The measurement of the crosstalk between the antenna and the interferometer shows a maximal transmission of approximately −20 dB at 4.7 GHz [see Fig. 5.10]. At the working frequency, the transmission between the two is with −44 dB even lower.

All in all, we see a slight decrease in transmission at the cross port, but still a good behaviour at the working frequency and only low crosstalk between antenna and interferometer. This shows, that the performance of the interferometer is only affected slightly by adding further parts and is therefore usable for further experiments, using transmons and antennas.

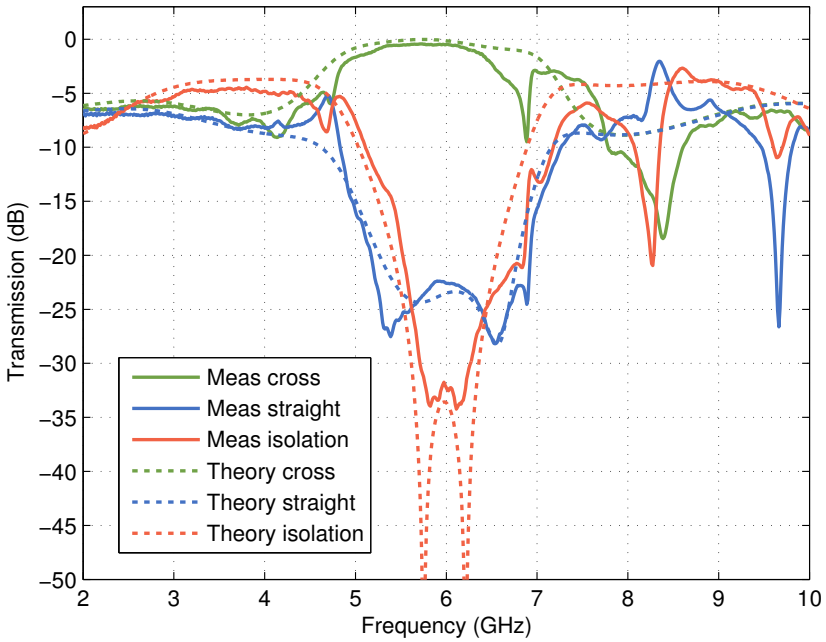

Figure 5.9: Measurement of the interferometer with two transmon sites and one antenna in comparison to the theory of that interferometer.

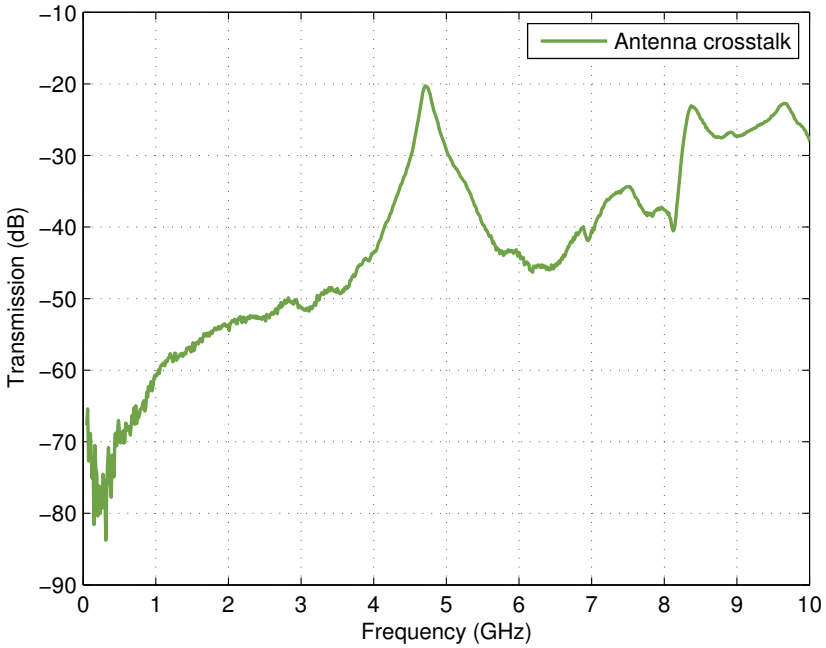

Figure 5.10: Measurement of the crosstalk between the antenna and the interferometer.

6. Summary and Outlook

In this thesis, we perform simulations of beam splitters and interferometers and measurements of the latter. With improvements to the measurement setup, such as, new cables in the cryostat, a new measurement box, new on board SMP connectors and changes in the PCB layout and soldering process, we are able to measure on-chip interferometers. The measured interferometers prove to be well predicted by theoretical calculations and by simulations. The isolation and straight transmission through the interferometers are well below $-20\,\mathrm{dB}$ at their working frequency, which is promising for future applications. The measurements included interferometers with long and short joints between the two beam splitters and an interferometer with an antenna and spaces for the placement of transmon qubits. The latter proved, that the addition of further parts of the phase gate does not impair the performance of the interferometer significantly. With the help of simulations, we can explain additional resonant features in the measurements, which stem from a mode in the substrate of the chip. We are also able to validate ideas for further improvements of the devices. For example, the simulations predict, that it is possible to suppress these additional resonant features by implementing on-chip vias or cutting of parts of the substrate and coating the edges with metal.

Thanks to the good performance of our interferometers, measurements of interferometers with transmon qubits inside the joints between the two beam splitters have already started and will be further investigated in the future. Later on, we can cascade a single photon source and an interferometer with transmon qubits to operate the phase gate. With this setup, we can then aim to measure the photon number dependent phase shift induced by the qubit and, in this way, benchmark the performance of the controlled phase gate. It is also of interest, to implement on-chip via production in order to validate the simulation results concerning the suppression of the chip modes.

A. Design parameters

This part gives an overview of the design parameters used for the structures investigated in this thesis.

Z_0	$50\,\Omega$
$Z_0/\sqrt{2}$	$35.4\,\Omega$
thickness of silicon layer H	$250\,\mu m$
thickness of niobium layer d	$100\,nm$
Width of gap G ($50\,\Omega$)	$20\,\mu m$
Width of gap G ($35.4\,\Omega$)	$20\,\mu m$
Width of inner conductor W ($50\,\Omega$)	$34.41\,\mu m$
Width of inner conductor W ($34.4\,\Omega$)	$125.2\,\mu m$
$\lambda_{work}/4(50\,\Omega)$	$5173\,\mu m$
$\lambda_{work}/4(35.4\,\Omega)$	$5205\,\mu m$

Bibliography

[1] R. J. Schoelkopf and S. M. Girvin, "Wiring up quantum systems", Nature **451**, 664–669 (2008).

[2] A. Blais, R.-S. Huang, A. Wallraff, S. M. Girvin, and R. J. Schoelkopf, "Cavity quantum electrodynamics for superconducting electrical circuits: An architecture for quantum computation", Phys. Rev. A **69**, 062320 (2004).

[3] E. Lucero, R. Barends, Y. chen, J. Kelly, M. Mariantoni, A. Megrant, P. O'Malley, D. Sank, A. Vainsencher, J. Wenn, T. White, Y. Yin, A. N. Cleland, and J. M. Martinis, "Computing prime factor with a Josephson phase qubit quantum procsessor", Nature **8**, 719–732 (2012).

[4] A. A. Houck, H. E. Türeci, and J. Koch, "On-chip quantum simulation with superconducting circuits", Nature **8**, 292–299 (2012).

[5] J. Clarke and F. K. Wilhelm, "Superconducting quantum bits", Nature **453**, 1031–1042 (2008).

[6] J. Koch, T. Yu, J. Gambetta, A. Houck, D. Schuster, J. Majer, A. Blais, M. Devoret, S. Girvin, and R. Schoelkopf, "Charge-insensitive qubit design derived from the Cooper pair box", Phys. Rev. A **76**, 042319 (2007).

[7] S. Haroche, "Nobel Lecture: Controlling photons in a box and exploring the quantum to classical boundary", Rev. Mod. Phys. **85**, 1083–1102 (2013).

[8] H. Walther, B. T. H. Varcoe, B.-G. Englert, and T. Becker, "Cavity quantum electrodynamics", Rep. Prog. Phys. **69**, 1325–1382 (2006).

[9] A. Wallraff, D. I. Schuster, A. Blais, L. Frunzio, R.-S. Huang, J. Majer, S. Kumar, S. M. Girvin, and R. J. Schoelkopf, "Strong coupling of a single photon to a superconducting qubit using circuit quantum electrodynamics", Nature **431**, 162–167 (2004).

[10] T. Niemczyk, F. Deppe, H. Huebl, E. P. Menzel, F. Hocke, M. J. Schwarz, J. J. Garcia-Ripoll, D. Zueco, T. Hümmer, and E. Solano, "Circuit quantum electrodynamics in the ultrastrong-coupling regime", Nature Phys. **6**, 772–776 (2010).

[11] C. Rigetti, J. M. Gambetta, S. Poletto, B. L. T. Plourde, J. M. Chow, A. D. Córcoles, J. A. Smolin, S. T. Merkel, J. R. Rozen, and G. A. Keefe, "Superconducting qubit in a waveguide cavity with a coherence time approaching 0.1 ms", Phys. Rev. B **86**, 100506 (2012).

[12] M. H. Devoret and R. J. Schoelkopf, "Superconducting Circuits for Quantum Information: An Outlook", Science **339**, 1169–1174 (2013).

[13] Y. Makhlin, G. Schön, and A. Shnirman, "Quantum-state engineering with Josephson-junction devices", Rev. Mod. Phys. **73**, 357–400 (2001).

[14] K. D. Osborn, J. A. Strong, A. J. Sirois, and R. W. Simmonds, "Frequency-Tunable Josephson Junction Resonator for Quantum Computing", IEEE Transactions on Applied Superconductivity **17**, 166–168 (2007).

[15] J. L. O'Brien, "Optical Quantum Computing", Science **318**, 1467 (2007).

[16] D. M. Pozar, *Microwave Engineering* (John Wiley & Sons, Inc., 2005).

[17] *TX-LINE 2003*, National Instruments AWR (http://www.awrcorp.com/products/optional-products/tx-line-transmission-line-calculator).

[18] R. N. Simons, *Coplanar Waveguide Circuits, Components, and Systems*, Wiley Series in Microwave and Optical Engineering (Wiley, Newark, NJ, 2001).

[19] *Simulations performed with CST microwave studio* (www.cst.com).

[20] M. T. Heath, *Scientific Computing: An Introductory Survey* (McGraw-Hill Higher Education, 1996).

[21] K. Kuang, F. Kim, and S. Cahill, *RF and Microwave Microelectronics Packaging* (Springer US, 2009).

[22] F. Loacker, "Design and Characterization of a Superconducting Beam Splitter for Quantum Information Processing", Master's thesis, Technische Universität München (2013).

[23] C. Schneider, "On-chip Superconducting Microwave Beamsplitter", Master's thesis, Technische Universität München (2014).

[24] E. P. Menzel, "Propagating Quantum Microwaves: Dual-path State Reconstruction and Path Entanglement", Ph.D. thesis, Technische Universität München (2013).

Acknowledgements

With this, I would like to thank

- Prof. Dr. Rudolf Gross for giving me the opportunity to perform my master's thesis at the Walther-Meißner-Institut.
- Dr. Edwin Menzel for his support as my supervisor. Working with you was great and I was able to learn a lot from your knowledge about measurement setup and physics in general. Thanks for taking the time for questions and discussions.
- Peter Eder for great support as well. I really enjoyed the short time we worked together.
- Dr. Frank Deppe for good discussions and for the help he gave me during my work at the Walther-Meißner-Institut.
- Friedrich Wulschner for always having a friendly ear for open questions or fabrication and measurement issues.
- Christian Schneider for a great year of working together.
- The qubit group for good discussions and a nice working atmosphere.
- My family for endless support in whatever I want to do, for always being there if I want to talk and for the good times we have.